

**Variational regional inverse modeling of reactive species emissions
with PYVAR-CHIMERE-v2019**

Audrey Fortems-Cheiney¹, Isabelle Pison¹, Grégoire Broquet¹, Gaëlle Dufour², Antoine Berchet¹,
Elise Potier¹, Adriana Coman², Guillaume Siour², and Lorenzo Costantino²

¹Laboratoire des Sciences du Climat et de l'Environnement, LSCE-IPSL (CEA-CNRS-UVSQ),
Université Paris-Saclay, 91191 Gif-sur-Yvette, France.

²Laboratoire Interuniversitaire des Systèmes Atmosphériques, UMR CNRS 7583, Université Paris
Est Créteil et Université Paris Diderot, Institut Pierre Simon Laplace, Créteil, France.

Abstract

Up-to-date and accurate emission inventories for air pollutants are essential for understanding their role in the formation of tropospheric ozone and particulate matter at various temporal scales, for anticipating pollution peaks and for identifying the key drivers that could help mitigate their concentrations. This paper describes the Bayesian variational inverse system PYVAR-CHIMERE, which is now adapted to the inversion of reactive species. Complementarily with bottom-up inventories, this system aims at updating and improving the knowledge on the high spatio-temporal variability of emissions of air pollutants and their precursors. The system is designed to use any type of observations, such as satellite observations or surface station measurements. The potential of PYVAR-CHIMERE is illustrated with inversions of both CO and NO_x emissions in Europe, using the MOPITT and OMI satellite observations, respectively. In these cases, local increments on CO emissions can reach more than +50%, with increases located mainly over Central and Eastern Europe, except in the south of Poland, and decreases located over Spain and Portugal. The illustrative cases for NO_x emissions also lead to large local increments (> 50%), for example over industrial areas (e.g., over the Po Valley) and over the Netherlands. The good behavior of the inversion is shown through statistics on the concentrations: the mean bias, RMSE, standard deviation and correlation between the simulated and observed concentrations. For CO, the mean bias is reduced by about 27% when using the posterior emissions, the RMSE and the standard deviation are reduced by about 50% and the correlation is strongly improved (0.74 when using the posterior emissions against 0.02); for NO_x, the mean bias is reduced by about 24%, the RMSE and the standard deviation are reduced by about 7% but the correlation is not improved. We reported strong non-linear relationships between NO_x emissions and satellite NO₂ columns, now requiring a fully comprehensive scientific study.

1. Introduction

The degradation of air quality is a worldwide environmental problem: 91% of the world's population have breathed polluted air in 2016 according to the World Health Organization (WHO), resulting in 4.2 millions of premature deaths every year [WHO, 2016]. The recent study of Lelieveld et al. [2019] even suggests that the health impacts attributable to outdoor air pollution are substantially higher than previously assumed (with 790,000 premature deaths in the 28 countries of the European Union against the previously estimated 500,000 [EEA, 2018]). The main regulated primary (i.e. directly emitted in the atmosphere) anthropogenic air pollutants are carbon monoxide (CO), nitrogen oxides ($\text{NO}_x = \text{NO} + \text{NO}_2$), sulfur dioxide (SO_2), ammonia (NH_3), volatile organic compounds (VOCs), and primary particles. These primary air pollutants are precursors of secondary (i.e. produced in the atmosphere through chemical reactions) pollutants such as ozone (O_3) and Particulate Matter (PM), which are also threatening to both human health and ecosystems. Monitoring concentrations and quantifying emissions are still challenging and limit our capability to forecast air quality to warn population and to assess i) the exposure of population to air pollution and ii) the efficiency of mitigation policies.

Bottom-up (BU) inventories are built in the framework of air quality policies such as The Convention on Long-Range Transboundary Air Pollution (LRTAP, <http://www.unece.org>) for air pollutants. Based on national annual inventories, research institutes compile gridded global or regional, monthly inventories (mainly for the US, Europe and China) with a high spatial resolution (currently regional or city scale inventories are typically finer than $0.1^\circ \times 0.1^\circ$). These inventories are constructed by combining available (economic) statistics data from different detailed activity sectors with the most appropriate emission factors (defined as the average emission rate of a given species for a given source or process, relative to the unit of activity in a given administrative area). It is important to note that the activity data (often statistical data) has an inherent uncertainty and that its reliability may vary between countries or regions. In addition, the emission factors bear large uncertainties in their quantification [Kuenen et al., 2014; EMEP/EEA, 2016; Kurokawa et al., 2013]. Moreover, these inventories are often provided at the annual or monthly scale with typical temporal profiles to build the weekly, daily and hourly variability of the emissions. The combination of uncertain activity data, emission factors and emission timing can be a large source of uncertainties, if not errors, for forecasting or analyzing air quality [Menut et al., 2012]. Finally, since updating the inventories and gathering the required data for a given year is costly in time, manpower and money, only a few institutes have offered estimates of the gaseous pollutants for each year since 2011 (i.e, European Monitoring and Evaluation Programme EMEP updated until the year 2017, MEIC updated until the year 2017 to our knowledge). Nevertheless, using knowledge

72 from inventories and air quality modeling, emissions have been mitigated. For example, from 2010
73 to nowadays, emissions in various countries have been modified and/or regional trends have been
74 reversed downwards (e.g., the decrease of NO_x emissions over China since 2011 [de Foy et al.,
75 2016]), leading to significant changes in the atmospheric composition. Consequently, the
76 knowledge of precise and updated budgets, together with seasonal, monthly, weekly and daily
77 variations of gaseous pollutants driven, amongst other processes, by the emissions are essential for
78 understanding their role in the formation of tropospheric ozone and PMs at various temporal scales,
79 for anticipating pollution peaks and for identifying the key drivers that could help mitigate these
80 concentrations.

81
82 In this context, complementary methods have been developed for estimating emissions using
83 atmospheric observations. They operate in synergy between a chemistry-transport model (CTM)
84 which links the emissions to the atmospheric concentrations, atmospheric observations of the
85 species of interest, and statistical inversion techniques. A number of studies using inverse modeling
86 were first carried out for long-lived species such as greenhouses gases (GHGs) (e.g., carbon dioxide
87 CO₂ or methane CH₄) at the global or continental scales [Hein et al., 1997; Bousquet et al. 1999],
88 using surface measurements. Later, following the development of monitoring station networks, the
89 progress of computing power, and the use of inversion techniques more appropriate to non-linear
90 problems, these methods were applied to shorter-lived molecules such as CO. For these various
91 applications (e.g., for CO₂, CH₄, CO), the quantification of sources was solved at the resolution of
92 large regions [Pétron et al., 2002]. Finally, the growing availability and reliability of observations
93 since the early 2000s (in-situ surface data, remote sensing data such as satellite data), the
94 improvement of the global CTMs, of the computational capacities and of the inversion techniques
95 have increased the achievable resolution of global inversions, up to the global transport model grid
96 cells, i.e. typically with a spatial resolution of several hundreds of square kilometers [Stavrakou and
97 Muller, 2006; Pison et al., 2009; Fortems-Cheiney et al., 2011; Hooghiemstra et al., 2012; Yin et
98 al., 2015; Miyazaki et al., 2017, Zheng et al., 2019].

99
100 Today, the scientific and societal issues require an up-to-date quantification of pollutant emissions
101 at a higher spatial resolution than the global one and imply to widely use regional inverse systems.
102 However, although they are suited to reactive species such as CO and NO_x, and their very large
103 spatial and temporal variability, they have hardly been used to quantify pollutant emissions. Some
104 studies inferred NO_x [Pison et al., 2007; Tang et al., 2013] and VOC emissions [Koohkan et al.,
105 2013] from surface measurements. Konovalov et al. [2006, 2008, 2010], Mijling et al. [2012, 2013],
106 van der A et al. [2008], Lin et al. [2012] and Ding et al. [2017] have also shown that satellite

107 observations are a suitable source of information to constrain NO_x emissions. These regional
108 inversions using satellite observations were often based on Kalman Filter (KF) schemes [Mijling et
109 al., 2012, 2013; van der A et al., 2008; Lin et al., 2012; Ding et al., 2017].

110

111 Variational inversion systems allow solving for high dimensional problems, typically solving for
112 the fluxes at high spatial and temporal resolution, which can be critical to fully exploit satellite
113 images. Here, we present the Bayesian variational atmospheric inversion system PYVAR-
114 CHIMERE for the monitoring of anthropogenic emissions of reactive species at the regional scale.
115 It is based on the Bayesian variational assimilation code PYVAR [Chevallier et al. 2005] and on the
116 regional state-of-the-art CTM CHIMERE [Menut et al., 2013; Mailler et al., 2017]. CHIMERE is
117 dedicated to the study of regional atmospheric pollution events [e.g., Ciarelli et al., 2019; Menut et
118 al., 2020], included in the operational ensemble of the Copernicus Atmosphere Monitoring Service
119 (CAMS) regional services. The main strengths of PYVAR-CHIMERE come from the strengths of
120 CHIMERE and from its high modularity for the definition of the control vector. CHIMERE is
121 indeed an extremely flexible code, in particular for the definition of the chemical scheme.

122 The PYVAR-CHIMERE system takes advantage of the previous developments for the
123 quantification of fluxes of long-lived GHG species such as CO_2 [Broquet et al., 2011] and CH_4
124 [Pison et al., 2018] at the regional to the local scales, but now solves for reactive species such as CO
125 and NO_x . It has also a better level of robustness, clarity, portability, and modularity than these
126 previous systems. Variational techniques require the adjoint of the model to compute the sensitivity
127 of simulated atmospheric concentrations to corrections of the fluxes. CHIMERE is one of the few
128 CTMs for which the adjoint has been coded. For global models, they include: GEOS-CHEM
129 [Henze et al., 2007], IMAGES [Stavrakou and Muller, 2006], TM5 [Krol et al., 2008], GELKA
130 [Belikov et al., 2016] and LMDz [Chevallier et al., 2005; Pison et al., 2009] ; for limited-area
131 models they include: CMAQ [Hakami et al., 2007], EURAD-IM [Elbern et al., 2007],
132 RAMS/CTM-4DVAR [Yumimoto et Uno, 2006], WRF-CO2 4D-Var [Zheng et al., 2018]).

133

134 The principle of variational atmospheric inversion and the configuration of PYVAR-CHIMERE are
135 described in Section 2 and in Section 3, respectively. Details about the forward, tangent-linear and
136 adjoint codes of CHIMERE are also given. Then, the potential of PYVAR-CHIMERE is illustrated
137 in Section 4 with the optimization of European CO and NO_x emissions, constrained by observations
138 from the Measurement of Pollution in the Troposphere (MOPITT) and from the Ozone Monitoring
139 Instrument (OMI) satellite instruments, respectively.

140

141

2. Principle of Bayesian variational atmospheric inversion

In what follows, we use the notations and equations used in the inverse modeling community [Rayner et al., 2019]. The Bayesian variational atmospheric inversion method adjusts a set of control parameters, including parameters related to the emissions whose estimate is the primary target of the inversion.

The prior information about the parameters \mathbf{x} to be optimized during the inversion process is given by the vector \mathbf{x}^b . The parameters to be optimized can be surface fluxes but may also include initial or boundary conditions for example, as explained in Section 3.4. The adjustments are applied to prior values, usually taken, for the emissions, from pre-existing BU inventories. The principle is to minimize, on the one hand, the departures from the prior estimates of the control parameters, which are weighted by the uncertainties in these estimates (called hereafter “prior uncertainties”), and, on the other hand, the differences between simulated and observed concentrations, which are weighted by all other sources of uncertainties explaining these differences (called hereafter all together “observation errors”). In statistical terms, the inversion searches for the most probable estimate of the control parameters given their prior estimates, observations, CTM and their associated uncertainties. The solution, which will be called posterior estimate, is found by the iterative minimization of a cost function J [Talagrand et al., 1997], defined as:

$$J(\mathbf{x}) = (\mathbf{x} - \mathbf{x}^b)^T \mathbf{B}^{-1}(\mathbf{x} - \mathbf{x}^b) + (H(\mathbf{x}) - \mathbf{y})^T \mathbf{R}^{-1}(H(\mathbf{x}) - \mathbf{y}) \quad (\text{Eq. 1})$$

H is the non-linear observation operator that projects the control vector \mathbf{x} onto the observation space. In most of the variational atmospheric inversion cases (such as those described in Section 4), the observation operator includes the operations performed by the CTM in linking the emissions to the concentrations and any other transformation to compute the simulated equivalent of the observations such as an interpolation or an extraction and averaging of the simulated concentration fields (see Section 3.5). The observations in \mathbf{y} could be surface measurements and/or remote sensing data such as satellite data. The prior uncertainties and the observation errors are assumed to be unbiased and to have a Gaussian distribution. Consequently, the prior uncertainties are characterized by their covariance matrix \mathbf{B} and the observation errors are characterized by their covariance matrix \mathbf{R} . By definition, the observation errors combine errors in both the data and the observation operator, in particular measurement errors and errors in the conversion of satellite measurement into concentration data, errors from the CTM, representativity errors due to the comparison between point measurements and gridded models or due to the representation of the fluxes as gridded maps at a given spatial resolution, and aggregation errors associated with the optimization of emissions at a given spatial and/or temporal resolution (as specified in the control vector) that is different from (usually coarser than) that of the CTM [Wang et al., 2017].

177

178 For inversions with observation and control vectors having a high dimension, the minimum of J
 179 cannot be found analytically due to computational limitations. It can be reached iteratively with a
 180 descent algorithm. In this case, the iterative minimization of J is based on a gradient method. J is
 181 calculated with the forward observation operator (including the CTM) and its gradient relative to
 182 the control parameters \mathbf{x} is provided by the adjoint of the observation operator (including the adjoint
 183 of the CTM). The gradient is defined as:

$$184 \nabla J(\mathbf{x}) = \mathbf{B}^{-1}(\mathbf{x} - \mathbf{x}^b) + H^* \mathbf{R}^{-1}(H(\mathbf{x}) - \mathbf{y}) \text{ (Eq. 2)}$$

185 where H^* is the adjoint of the observation operator.

186

187 The high non-linearity of the chemistry for reactive species makes it difficult to use its tangent-
 188 linear to approximate the actual observation operator, and, more generally, it makes the inversion
 189 problem highly non-linear. Therefore, in PYVAR-CHIMERE, we use the M1QN3 limited memory
 190 quasi-Newton minimization algorithm [Gilbert and Lemaréchal, 1989], which relies on the actual
 191 CHIMERE non-linear model to compute J at each iteration of the minimization. As most quasi-
 192 Newton methods, it requires an initial regularization of \mathbf{x} , the vector to be optimized, for better
 193 efficiency. We adopt the most generally used regularization, made by minimizing in the space
 194 defined by:

$$195 \chi = \mathbf{B}^{\frac{1}{2}}(\mathbf{x} - \mathbf{x}^b) \text{ (Eq. 3)}$$

196 instead of the control space defined by \mathbf{x} . Although more advanced regularizations can be chosen,
 197 the minimization with χ is preferred for its simplifying the equation to solve. In the χ -space,
 198 Equation 2 can be re-written as follows:

$$199 \nabla J\chi = \chi + \mathbf{B}^{\frac{1}{2}} H^* (\mathbf{R}^{-1}(H(\mathbf{x}) - \mathbf{y})) \text{ (Eq. 4)}$$

200

201 The criterion for stopping the algorithm is based on a threshold set on the ratio between the final
 202 and initial gradient norms or on the maximum number of iterations to perform. As shown in Figure
 203 1, the minimization algorithm repeats the forward-adjoint cycle to get an estimate close to the
 204 optimal solution of the inversion problem for the control parameters. This approximation of the
 205 optimal estimate is found by satisfying the convergence criteria of the minimizer with a given
 206 reduction of the norm of the gradient of J . Nevertheless, due to the non-linearity of the problem, the
 207 minimization may reach a local minimum only, instead of the global minimum.

208

209 Finally, the calculation of the uncertainty in the estimate of emissions from the inversion, known as
 210 “posterior uncertainty”, is challenging in a variational inverse system [Rayner et al., 2019]. Even

though the posterior uncertainty can be explicitly written in various analytical forms, it requires the inversion of matrices that are too large to invert given the current computational resources in our variational approach. As a trade-off between computing resources and comprehensiveness, the analysis error may be evaluated by an approach based on a propagation of errors through sensitivity tests (e.g., as in Fortems-Cheiney et al., [2012]). It can also be estimated through a Monte Carlo Ensemble [Chevallier et al., 2007], implemented in PYVAR. Nevertheless, it should be noted that the cost of the Monte Carlo experiments used to derive these posterior uncertainties is huge.

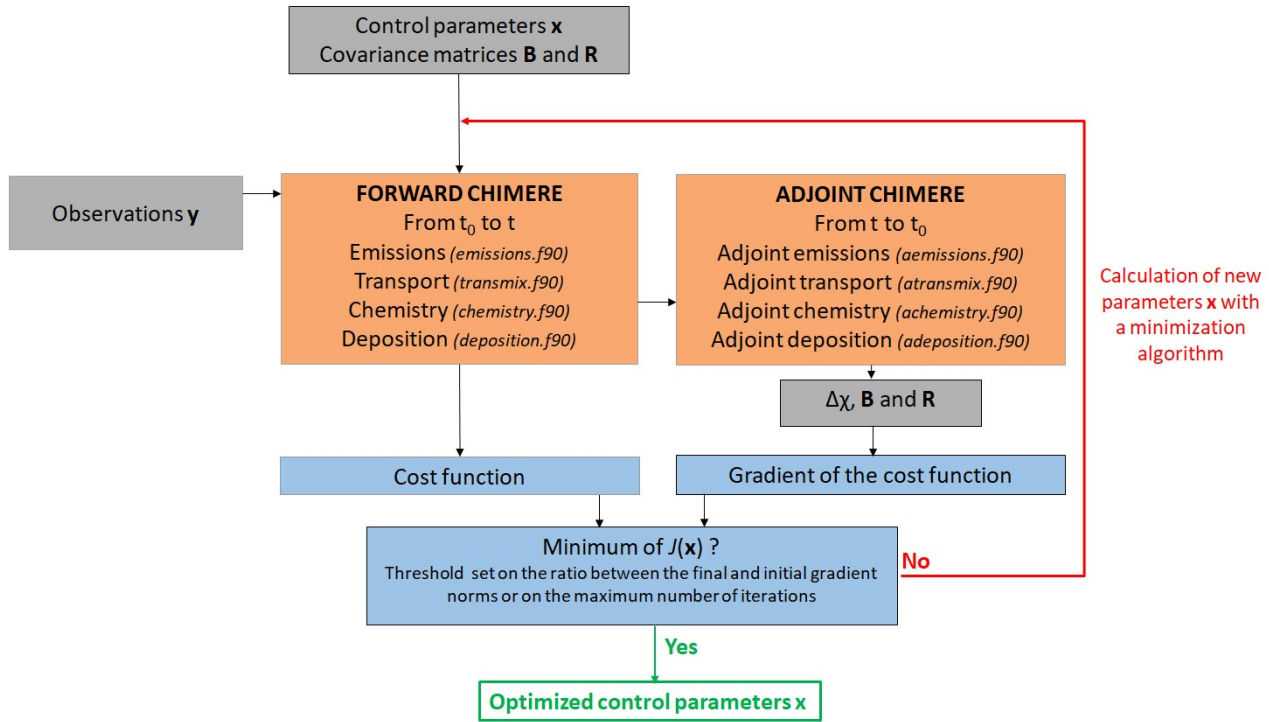


Figure 1. Simplified scheme of the iterative minimization in PYVAR-CHIMERE. PYVAR, CHIMERE and text sources are displayed in blue, in orange and in grey, respectively.

3. The PYVAR-CHIMERE configuration

3.1. PYVAR adapted to CHIMERE

The PYVAR-CHIMERE inverse modeling system is based on the Bayesian variational assimilation code PYVAR [Chevallier et al. 2005] and on a previous inversion system coupled to CHIMERE [Pison et al., 2007]. PYVAR is an ensemble of Python scripts, which deals with preparing the vectors and the matrices for the inversion, drives the required Fortran codes of the transport model and computes the minimization of the cost function to solve the inversion. Previously used for global inversions with the LMDz model [e.g., Pison et al., 2009; Chevallier et al., 2010; Fortems-Cheiney et al., 2011; Yin et al., 2015; Locatelli et al., 2015; Zheng et al., 2019], PYVAR has been adapted to CHIMERE with an adjoint code without chemistry by Broquet et al. [2011]. In order to couple PYVAR to the new state-of-the-art version of CHIMERE (see Section 3.2), to include

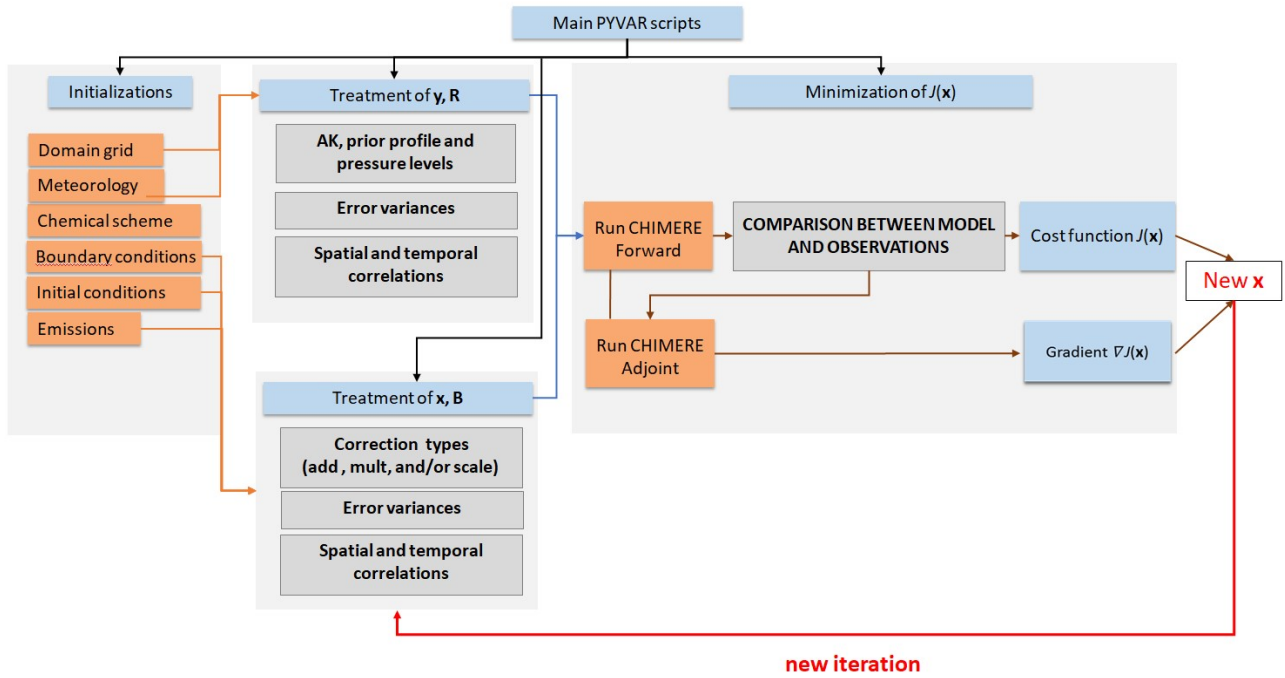
chemistry, and to increase its modularity, flexibility and clarity, the new system described here has been developed. It includes elements of the inversion system (coded in Fortran90) of Pison et al. [2007].

3.2. Development and parallelization of the adjoint and tangent-linear codes of CHIMERE

To compute the sensitivity of simulated atmospheric concentrations to corrections to the fluxes, the adjoint of CHIMERE has been developed. Originally, the sequential adjoint was coded [Menut et al., 2000; Menut et al., 2003; Pison et al., 2007]. The adjoint has been coded by hand line by line, following the principles formulated by Talagrand [1997]. It contains exactly the same processes as the CHIMERE forward model. The code has been parallelized, which required a redesigning of the entire code, associated with a full testing scheme (see Section 3.3). Furthermore, the tangent-linear (TL) code has been developed and validated (see Section 3.3). Changes have been implemented in the forward CHIMERE code embedded in PYVAR-CHIMERE to match requirements of the studies conducted with this system. These changes have been implemented in both the adjoint and the TL codes. Compared to the CHIMERE 2013 version [Menut et al., 2013], the most important of these changes are, regarding geometry, the possibility of polar domains and the use of the coordinates of the corners of the cells instead of only the centers, allowing the use of irregular grids. Regarding transport, the non-uniform Van Leer transport scheme on the horizontal has been implemented, which is consistent with the use of irregular grids. Finally, various switches have been added to keep the system consistent for GHG studies. For example, we can avoid going into the chemistry, deposition or wet deposition routines when the focused species do not require them (e.g., no chemistry for methane or carbon dioxide at a regional scale).

PYVAR-CHIMERE is currently implemented with a full module of gaseous chemistry. As a compromise between the robustness of the method for reactive species, the time required coding the adjoint and the computational cost with a full chemical scheme, the aerosols modules of CHIMERE have not been included in the adjoint of CHIMERE yet and are therefore not available in PYVAR-CHIMERE. The development and maintenance of the adjoint means that the version used is necessarily one or two versions behind the distributed CHIMERE version (<http://www.lmd.polytechnique.fr/chimere/>). It should also be noted that PYVAR-CHIMERE only infers anthropogenic emissions at this stage. The optimization of biogenic emissions, which are linearly interpolated at the sub-hourly scale in CHIMERE, is currently under development.

268 As an example, Figure 2 presents a simplified scheme of how PYVAR scripts are used to drive this
 269 version of CHIMERE for forward simulations and inversions using satellite observations.
 270



271
 272 **Figure 2.** Simplified scheme of how PYVAR scripts are used to drive CHIMERE for an inversion
 273 using satellite observations. PYVAR, CHIMERE and text sources are displayed in blue, in orange
 274 and in grey, respectively. “AK” refers to Averaging Kernels as detailed in Section 3.5.
 275

276 3.3. Accuracy of tangent-linear and adjoint codes

277 Different procedures have been implemented to test the accuracy of the TL and adjoint codes. To
 278 test the linearity of the TL, we compute a Taylor diagnostic. It consists in computing the TL at \mathbf{x}_0
 279 for given increments $\Delta\mathbf{x}$, $dH\mathbf{x}_0(\Delta\mathbf{x})$, then the TL at \mathbf{x}_0 for $\lambda \times \Delta\mathbf{x}$ with λ an arbitrary small number,
 280 $dH\mathbf{x}_0(\lambda\Delta\mathbf{x})$. Theoretically, if the TL is well coded, $\lambda dH\mathbf{x}_0(\Delta\mathbf{x}) = dH\mathbf{x}_0(\lambda\Delta\mathbf{x})$ by definition. In practice,
 281 the difference must be lower than 10 times the precision of the machine on which it is run.

282
 283 The adjoint code is also tested, by verifying that $\langle H.\Delta\mathbf{x}, H.\Delta\mathbf{x} \rangle = \langle \Delta\mathbf{x}, H^T H.\Delta\mathbf{x} \rangle$ where H^T stands for
 284 the adjoint at \mathbf{x} . What is actually computed is the ratio of the difference between the two scalar
 285 products to the second one and the accuracy of the computation. The difference should be a few
 286 times the precision of the machine on which it is run.

288 3.4. Definition of the control vector

289 The control vector is specified by the user in a text file. This file is formatted following Table 1.
 290 The parameters to be inverted may be fluxes and/or initial conditions and/or boundary concentration

291 conditions, at the grid-cell resolution or for one region encompassing up to the whole domain.
292 Several types of corrections can be applied, they are defined in the code as "add", "mult" or "scale".
293 Both the corrections "add" and "mult" are applied to gridded control variables. For correction type
294 "add", the control variables are increments added to the corresponding components of the model
295 inputs. For correction type "mult", the control variables are scaling factors multiplying the
296 corresponding components of the model inputs. The difference between the two options "add" and
297 "mult" plays a role when inverting fluxes which can switch from positive to negative values (like
298 CO₂ natural fluxes). For type "scale", the control variables are scaling factors applied to maps
299 different from the maps of emissions used as prior input of the forward model: for example, activity
300 maps can be used and scaled to get emissions; the obtained values are then added to the
301 corresponding components of the model inputs. With these various types, it is possible to define the
302 control variables as the budgets of emissions for different regions, types of activities, and/or
303 processes, which can thus be directly rescaled by the inversions, similarly to what is done in
304 systems where the control vector is not gridded [Wang et al., 2018]).

305

306 Different simple but efficient ways of building the error covariance matrix **B** are implemented in
307 PYVAR-CHIMERE. The variances and correlations are defined independently. The variances are
308 specified by the user through the specification of the values for the corresponding standard
309 deviation (i.e. the diagonal matrix of standard deviations Σ , Table 1) which can be made in terms of
310 fixed values ("fx") or percentages ("pc"). For correction types "mult" and "scale", as well as for
311 correction type "add" with a fixed value, the value is directly used as the uncertainty in the
312 corresponding components of the control vector. For correction type "add" with a percentage
313 provided, maps of standard deviation of uncertainty are built by applying this percentage to the
314 matching input fields (fluxes, initial conditions, boundary conditions). The user may also provide a
315 script to build personalized maps of variances.

316

317 Potential correlations between uncertainties in different types of control variables, e.g. between
318 fluxes and boundary conditions, and correlations between uncertainties in different species, e.g.
319 between fluxes of CO and NO_x, are not coded yet. Such correlations increase the observation
320 constraint on the emissions in the inversion process by transferring information from one species to
321 the other. The level (and sometimes the sign) and thus the impact on the inversion of such
322 correlations highly depends on the study cases, and are often debated due to the lack of precise
323 characterization of the uncertainties in inventories of anthropogenic emissions of GHG and
324 pollutants [Super et al. 2020]. Only correlations for a given type of control variable and a given
325 species are so far taken into account so that the **B** matrix is block diagonal. For a given type of

control variable and a given species (in the illustration in section 4.2.2: CO, NO or NO₂ fluxes), spatial and temporal correlations can be defined using correlation lengths through time L_t and space L_s . Those lengths are used to model temporal and/or spatial auto-correlations using an exponentially decaying function: the correlation r between parameters and at a given location but separated by duration $d(x_i, x_j)$, or at a given time but distant by $d(x_i, x_j)$ is given by $r(x_i, x_j) = \exp\left(\frac{-d(x_i, x_j)}{L}\right)$ (Eq. 5) where $L = L_T \vee L_S$ is the corresponding correlation length. There is no correlation between uncertainties in land and ocean flux. Note that the spatial correlations are computed for each vertical level independently when dealing with control variables with vertical resolution (3D fields of fluxes when accounting for emission injection heights, or boundary/initial conditions). Vertical correlations in the uncertainties in such variables have not been coded yet. Apart from this, the system assumes that temporal correlations and spatial correlations depend on the time lag and distance but not on the specific time and location of the corresponding parameters. It also assumes that the correlation between uncertainties at different locations and different time can be derived from the product of the corresponding autocorrelation in time and space.

Each block of \mathbf{B} can thus be decomposed based on Kronecker products: $\mathbf{B} = \sum C_t \otimes C_s \sum$ (Eq. 6) where \otimes is the Kronecker product, C_t and C_s are the temporal and spatial correlations, respectively. The calculations involving $\mathbf{B}^{1/2}$ (in Eq. 3, Eq. 4) are simplified in PYVAR-CHIMERE using the Eigen-decomposition of C_t and C_s . Its square root can be calculated according to: $C_t^{1/2} = V_{C_t} D_{C_t}^{1/2} V_{C_t}^T$ (Eq. 7) (and similarly for C_s), where V_{C_t} is the matrix with the Eigenvectors as columns, and D_{C_t} is the diagonal matrix of Eigenvalues of C_t . It is possible to chose a threshold under which the eigenvalues are truncated when computing the spatial correlations in order to save computation time and memory, but not when computing the temporal correlations.

Constrained species	Correction type : - Add - Mult - Scale	Spatial resolution	Temporal resolution (in hours)	Input to constrain: -Fluxes -Initial conditions -Lateral Boundary conditions -Top Boundary conditions	B variance coefficient: -fx -pc	Decorrelation time (in hours)	Decorrelation length on land (in km)	Decorrelation length on sea (in km)
CO	add	0.5°x0.5°	168	Fluxes	100 %	-	-	-
CO	add	0.5°x0.5°	1	Initial conditions	15%	-	-	-
CO	add	0.5°x0.5°	168	Lateral Boundary	15%	-	-	-

				conditions				
CO	add	0.5°x0.5°	168	Top Boundary conditions	15%	-	-	-
NO	add	0.5°x0.5°	24	Fluxes	50 %	-	50	50
NO	add	0.5°x0.5°	1	Initial conditions	15%	-	-	-
NO ₂	add	0.5°x0.5°	24	Fluxes	50 %	-	50	50
NO ₂	add	0.5°x0.5°	24	Initial conditions	15%	-	-	-

Table 1. Examples for the definition of the control vector and for the construction of the B matrix, as illustrated in Section 4.

3.5. Equivalents of the observations

During forward simulations, the equivalents of the components of \mathbf{y} (i.e, the equivalents of the individual data) are calculated by PYVAR-CHIMERE. It includes the CTM and an interpolation (see below the vertical interpolation from the model's grid to the satellite levels) or an extraction and averaging (e.g. extracting the grid cell matching the geographical coordinates of a surface station and averaging over one hour). As a compromise between technical issues such as the time required for reading/writing files, the observation operator H that generates the equivalent of the observations by the model (i.e. $H(\mathbf{x})$) has been so far partly embedded in the code of CHIMERE. It makes it easier to use finer time intervals than available in the usual hourly outputs of CHIMERE to compute the required information (e.g., within the finer CTM physical time steps).

To make comparisons between simulations and satellite observations, the simulated vertical profiles are first interpolated on the satellite's levels (with a vertical interpolation on pressure levels) in CHIMERE. Then, the averaging kernels (AKs), when available, are applied to represent the vertical sensitivity of the satellite retrieval. Two types of formula, depending on the satellite observations used, have been detailed in PYVAR-CHIMERE for the use of AKs: $\mathbf{c}_m = \mathbf{AK} \cdot \mathbf{c}_{m(o)}$ (Eq. 8) or $\mathbf{c}_m = \mathbf{x}_a + \mathbf{AK}(\mathbf{c}_{m(o)} - \mathbf{x}_a)$ (Eq. 9) where \mathbf{c}_m is the modeled column, AK contains the averaging kernels that can be provided in the form of vector (e.g., OMI product) or matrix (e.g., MOPITT product), \mathbf{x}_a is the prior state vector (provided together with the AKs when relevant) and $\mathbf{c}_{m(o)}$ is the vertical distribution of the original model partial columns interpolated to the pressure grid of the AKs.

3.6. Numerical language

The PYVAR code is in Python 2.7, the CHIMERE CTM is coded in Fortran90. The CTM requires several numerical tools, compilers and libraries. The PYVAR-CHIMERE system was developed and tested using the software versions as described in Table 2.

		URL	Version
Software	Python	https://www.python.org/downloads/	2.7
	Fortran compiler ifort	https://software.intel.com/en-us/fortran-compilers	Composer-xe-2013.2.146
Libraries or packages	UnidataNetCDF	https://www.unidata.ucar.edu/	3
	Open MPI	https://www.open-mpi.org/	1.10.5
	GRIB_API	https://confluence.ecmwf.int/display/GRIB/Releases	1.14
	nco	http://nco.sourceforge.net/#Source	4.6.3

Table 2. URL addresses for the development and the use of the PYVAR-CHIMERE system and its modules.

PYVAR-CHIMERE's computation time for one node of 10 CPUs is about 4h for 1 day of inversion (with ~10 iterations) for the European domain size of 101 (longitude) x 85 (latitude) x 17 (vertical levels) used in Section 4. As described in Menut et al. [2013] for CHIMERE, the model parallelization results from a Cartesian division of the main geographical domain into several sub-domains, each one being processed by a worker process. To configure the parallel sub-domains, the user has to specify two parameters in the model parameter file: the number of sub-domains for the zonal and meridian directions. The total number of CPUs used is therefore the product of these two numbers plus one for the master process. The optimal number of CPUs for the parallelization of the transport scheme depends on the size of the tiles and also of the technical characteristics of the machine, because of the time required to exchange halos.

4. Potential of PYVAR-CHIMERE for the inversion of CO and NO_x emissions

The potential of the PYVAR-CHIMERE system to invert emissions of reactive species is illustrated with the inversion of CO and NO_x anthropogenic emissions in Europe respectively based on MOPITT CO data and OMI NO₂ data. We have chosen to present an illustration of CO inversion over seven days, the first week of March 2015. Considering the short lifetime of NO_x of a few hours [Valin et al., 2013; Liu et al., 2016], we have chosen to present illustration of NO_x inversion over one day, 19 February 2015. These particular periods have been chosen as they present a representative number of super-observations during winter, and as the emissions are high during that period. All the information required by the system to invert CO and NO_x emissions is listed in Table 1.

4.1. Data and model description

4.1.1. Observations

We use CO data from the MOPITT instrument [Deeter et al., 2019]. MOPITT has been flown onboard the NASA EOS-Terra satellite, on a low sun-synchronous orbit that crosses the equator at 10:30 and 22:30 LST. The spatial resolution of its observations is about $22 \times 22 \text{ km}^2$ at nadir. It has been operated nearly continuously since March 2000. MOPITT CO products are available in three variants: thermal-infrared TIR only, near-infrared NIR only and the multispectral TIR-NIR product, all containing total columns and retrieved profiles (expressed on a ten-level grid from the surface to 100 hPa). We choose to constrain CO emissions with the MOPITT surface product for our illustration. Among the different MOPITTv8 products, we choose to work with the multispectral MOPITTv8-NIR-TIR one, as it provides the highest number of observations, with a good evaluation against in situ data from NOAA stations [Deeter et al., 2019]. The MOPITTv8-NIR-TIR surface concentrations are sub-sampled into “super-observations” in order to reduce the effect of errors that are correlated between neighboring observations: we selected the median of each subset of MOPITT data within each $0.5^\circ \times 0.5^\circ$ grid-cell and each physical time step (about 5-10 minutes). After this screening, 8437 “super-observations” remain in the 7-day inversion (from 10667 raw observations). It is important to note that the potential of MOPITT to provide information at a high temporal resolution, up to the daily scale, is hampered by the cloud coverage (see the blanks in Figure 5b).

The observational constraint on NO_2 emissions comes from the OMI QA4ECV tropospheric columns [Muller et al., 2016; Boersma et al., 2016, Boersma et al., 2017]. The Ozone Monitoring Instrument (OMI), a near-UV/Visible nadir solar backscatter spectrometer, was launched onboard EOS Aura in July 2004. It has been flown on a 705 km sun-synchronous orbit that crosses the Equator at 13:30 LT. Our data selection follows the criteria of the OMI QA4ECV data quality statement. As the spatial resolution of the OMI data is finer than that of the chosen CHIMERE model grid ($13 \times 24 \text{ km}^2$ against $0.5^\circ \times 0.5^\circ$, respectively), the OMI tropospheric columns are sub-sampled into “super-observations” (median of the OMI data within the $0.5^\circ \times 0.5^\circ$ grid-cell and each physical time step and its corresponding AK).

4.1.2 CHIMERE set-up

CHIMERE is run over a $0.5^\circ \times 0.5^\circ$ regular grid (about $50 \times 50 \text{ km}^2$) and 17 vertical layers, from the surface to 200hPa (about 12km), with 8 layers within the first two kilometers. The domain includes 101 (longitude) x 85 (latitude) grid-cells (15.5°W - 35°E ; 31.5°N - 74°N , see Figure 3). CHIMERE is driven by the European Centre for Medium-Range Weather Forecasts (ECMWF) meteorological

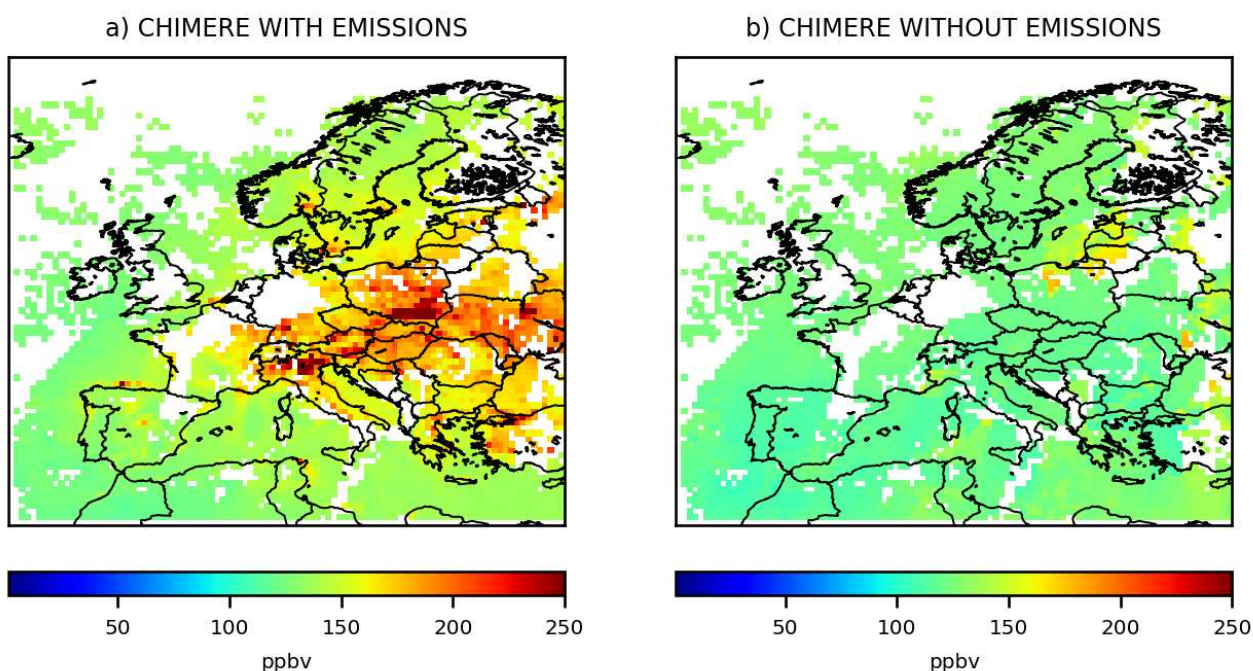
438 forecast [Owens and Hewson, 2018]. The chemical scheme used in PYVAR-CHIMERE is
439 MELCHIOR-2, with more than 100 reactions [Lattuati, 1997; CHIMERE 2017], including 24 for
440 inorganic chemistry. The prior anthropogenic emissions for CO and NO_x emissions are obtained
441 from the TNO-GCHco-v1 inventory [Super et al., 2020], the last update of the TNO-MACCII
442 inventory [Kuenen et al., 2014]. This inventory is based on the EMEP/Centre on Emission
443 Inventories and Projections (CEIP) official country reporting for air pollutants done in 2017. It is an
444 inventory at 6x6km² horizontal resolution. From the annual and national budgets, each sector is
445 assigned to a specific proxy to quantify the spatial variability of the emissions within each country.
446 Temporal profiles are also provided per Gridded Nomenclature For Reporting (GNFR) sector code
447 (variations due to the month, weekday and hour). Following the Generation of European Emission
448 Data for Episodes (GENEMIS) recommendations [Kurtenbach et al., 2001; Aumont et al., 2003],
449 NO_x emissions are speciated as 90% of NO, 9.2% of NO₂, and 0.8% of nitrous acid (HONO). The
450 TNO-GHGco-v1 inventory has been aggregated to the CHIMERE grid.

451

452 The prior anthropogenic emissions for VOCs are obtained from the EMEP inventory [Vestreng et
453 al., 2005; EMEP/CEIP website]. Biogenic emissions come from the Model of Emissions of Gases
454 and Aerosols from nature (MEGAN) [Guenther et al., 2006]. Different climatological values from
455 the LMDZ-INCA global model [Szopa et al., 2008] or from a Monitoring Atmospheric
456 Composition and Climate (MACC) reanalysis are used to prescribe concentrations at the lateral and
457 top boundaries and the initial atmospheric composition in the domain. Full access to and more
458 information about the MACC reanalysis data can be obtained through the MACC-II web site
459 (<http://www.copernicus-atmosphere.eu>). In order to ensure realistic fields of simulated CO and NO₂
460 concentrations from the beginning of the inversion period, runs have been preceded with a 10-day
461 spin-up.

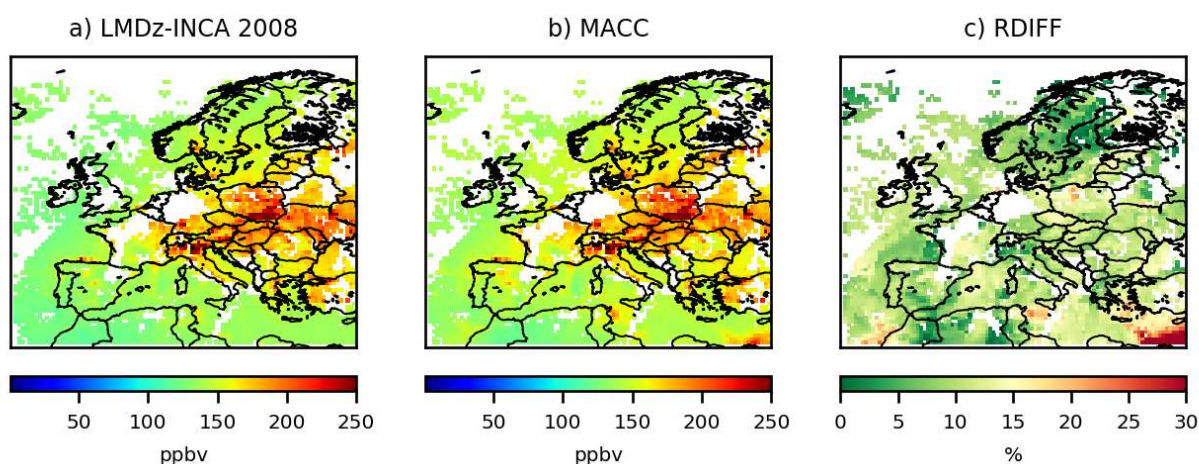
4.1.3. CO Sensitivity to emissions and to initial and boundary conditions

462 With its lifetime of about two months, CO could be strongly influenced by the initial and lateral
463 boundary conditions prescribed in the CTM. In fact, as seen in Figure 4b, initial and boundary
464 conditions provide a relatively flat background and the patterns which appear clearly over the
465 background are linked to surface emissions (Figure 4a). To characterize the uncertainties in the
466 concentration fields due to the initial and lateral boundary conditions, we performed a sensitivity
467 test by using either climatological values from LMDZ-INCA or a MACC reanalysis: maximum
468 relative differences in concentrations of about 15% over continental land are estimated (Figure 4c).
469 The errors assigned to initial and boundary conditions in Section 4.2.2 are based on this sensitivity
470 test.



471

Figure 3. Mean CO surface concentrations from the 1st to the 7th, March 2015 simulated by CHIMERE a) with anthropogenic and biogenic emissions, and b) without emissions, in ppbv, at the 0.5°x0.5° grid-cell resolution.



472

Figure 4. Mean CO surface concentrations from the 1st to the 7th, March 2015 simulated by CHIMERE using for initial and boundary conditions, a) the climatological values from the LMDZ-INCA global model b) the climatological values from a MACC reanalysis, in ppbv, and c) the relative differences between these two simulations , in %, at the 0.5°x0.5° grid-cell resolution.

4.1.4. Comparison between CHIMERE and the observations

473

474

Large discrepancies (Figure 5d) are found between the MOPITT CO observations (Figure 5b) and the prior simulation by CHIMERE over Europe (Figure 5a). For the first week of March 2015, CO

475 concentrations are generally under-estimated by CHIMERE, particularly over Central and Eastern
 476 Europe (excepted in the south of Poland). On the contrary, CO concentrations seem to be over-
 477 estimated over Spain and Portugal. Large discrepancies are also found between the OMI NO₂ super-
 478 observations and the prior simulation by PYVAR-CHIMERE (Figure 6d), as already noticed by
 479 Huijnen et al. [2010], with an inter-comparison of NO₂ OMI-DOMINO tropospheric columns with
 480 an ensemble of European regional air quality models including CHIMERE. Over Europe, the prior
 481 simulation strongly underestimates the tropospheric columns over industrial areas (e.g., over the
 482 Netherlands and over Po Valley). These discrepancies might be due to different causes, which can
 483 all interact. A source of uncertainties is related to the observations. For example, satellite data inter-
 484 comparison studies reveal large differences between different retrievals of the same compound [Qu
 485 et al., 2020]. It can be explained by uncertainties from the CTM (e.g., through the underestimation
 486 of the atmospheric production or the underestimation of the species lifetime). It could also be
 487 explained by an underestimation of the anthropogenic emissions in the BU inventory.
 488

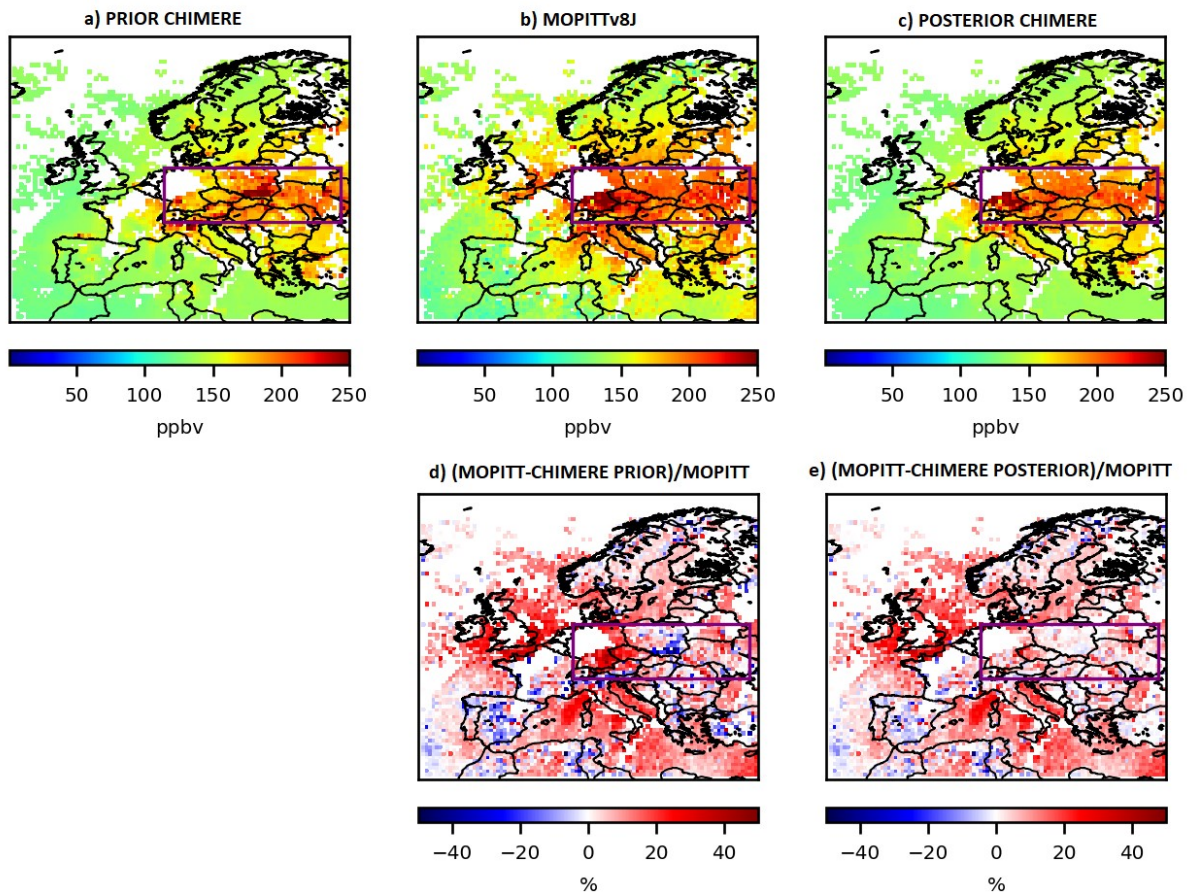


Figure 5. Mean CO collocated surface concentrations from the 1st to the 7th, March 2015 a) simulated by CHIMERE using the prior TNO-GHGco-v1 emissions and the climatological values from the LMDZ-INCA global model for initial and boundary conditions, b) observed by MOPITTv8-NIR-TIR and c) simulated by CHIMERE using the posterior emissions, in ppbv, at the

0.5°x0.5° grid-cell resolution. Relative differences between MOPITT and d) the prior CHIMERE simulation or e) the posterior CHIMERE simulation, in %. Statistics for the comparison between simulations and observations are given in Table 4 for the area in the purple box.

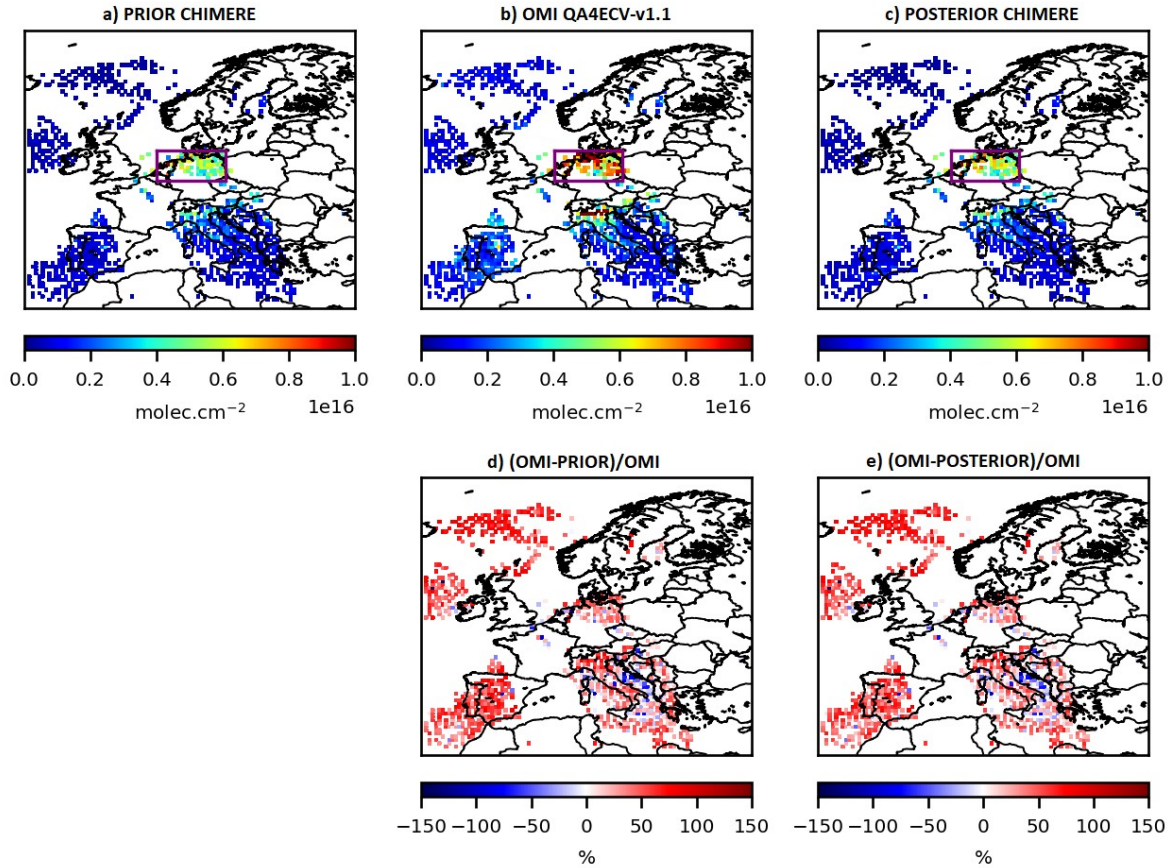


Figure 6. NO_2 collocated tropospheric columns a) simulated by CHIMERE using the prior TNO-GHGco-v1 emissions and the climatological values from the LMDZ-INCA global model for initial and boundary conditions, b) observed by OMI and c) simulated by CHIMERE using the posterior emissions, in $10^{16} \text{ molec.cm}^{-2}$, at the $0.5^\circ \times 0.5^\circ$ grid-cell resolution, the 19th, February 2015. Relative differences between OMI and d) the prior CHIMERE simulation or e) the posterior CHIMERE simulation, in %. Statistics for the comparison between simulations and observations are given in Table 5 for the area in the purple box.

4.2. Inversions

4.2.1. Control vector \mathbf{x}

For the CO inversion, the control vector \mathbf{x} is:

- the CO anthropogenic emissions at a 7-day temporal resolution, a $0.5^\circ \times 0.5^\circ$ (longitude, latitude) horizontal resolution, and over the first 8 vertical levels, i.e. for each of the corresponding $101 \times 85 \times 8$ grid cells,

- the CO lateral and top boundary conditions at a 7-day temporal resolution, at a $0.5^\circ \times 0.5^\circ$ (longitude, latitude) resolution and over the 17 vertical levels of CHIMERE, i.e. $(2 \times 101 + 2 \times 85) \times 17$ grid cells,
- the CO 3D initial conditions for the 1st March 2015 at 0:00 UTC, at a $0.5^\circ \times 0.5^\circ$ (longitude, latitude) resolution, and over the 17 vertical levels of CHIMERE.

Considering its short lifetime, there is no boundary conditions for NO₂. For the NO_x inversion, the control vector **x** is:

- the NO and NO₂ anthropogenic emissions at a 1-day temporal resolution, at a $0.5^\circ \times 0.5^\circ$ (longitude, latitude) resolution and over the first 8 vertical levels, i.e. for each of the corresponding $101 \times 85 \times 8$ grid cells,
- the NO and NO₂ 3D initial conditions for the 19th February 2015 at 0:00 UTC, at a $0.5^\circ \times 0.5^\circ$ (longitude, latitude) resolution and over the 17 vertical levels of CHIMERE.

4.2.2. Covariance matrices **B** and **R**

To our knowledge, there are few available studies dealing with the estimates of the uncertainties in gridded bottom-up emission inventories at the $0.5^\circ \times 0.5^\circ$ resolution or higher. The characterization of their statistics in the inversion configuration is consequently often based on crude assumptions from the inverse modelers. Defining the covariance matrices **B** and **R** is not an easy task, while incorrectly specifying these matrices has a very strong impact on the results of the inversion. Especially, the relative weights of **B** and **R**, and the spatial and temporal correlations in **B** influence the degree of freedom and the structure for the adjustments attempted by the inversion in the optimization process. Consequently, as an example for the NO_x inversion, different sensitivity tests described in Table 3 have been performed for the construction of the **B** matrix. For both the prior NO and NO₂ emissions at 1-day and 0.5° resolution, the prior error standard deviations are first assigned to 50% of the prior estimate of the emissions (test A), as in Souri et al. [2020]. Sensitivity tests have also been performed with prior error standard deviations assigned to 80 and 100% of the prior estimate of the emissions (test C and test D, respectively, Figure 8).

With prior error standard deviations set at 15% of the initial conditions, the changes in initial conditions are very small (not shown) and do not affect the posterior emissions (test B, Figure 8). As indicated in Section 3.4 and in Table 1, it is possible to use correlations in **B**, as in Broquet et al. [2011], in Broquet et al. [2013] and in Kadygrov et al. [2015]. We demonstrate the strong impact of spatial correlations, defined by an e-folding length of 50km over land and over the sea, on our inversions results (test E, Figure 8).

Name of the sensitivity tests	Prior error standard deviations in \mathbf{B}		Spatial correlation in \mathbf{B}	Number of iterations	Reduction of the norm of the gradient of J
	On prior emissions	On prior initial conditions			
A	50%	-	-	4	99%
B	50%	15%	-	6	98%
C	80%	15%	-	7	97%
D	100%	15%	-	6	95%
E	50%	15%	50km	5	92%

Table 3. Description of the different sensitivity tests performed for the construction of the \mathbf{B} matrix for the NO_x inversion.

Even though annual CO emissions in Western Europe may be well known, with uncertainties of 6% according to Super et al., [2020], larger uncertainties could affect Eastern Europe. Moreover, large uncertainties still affect bottom-up emission inventories at the 0.5° resolution: spatial disaggregation of the national scale estimates to provide gridded estimates causes a significant increase in the uncertainty for CO [Super et al., 2020]. For the inversion of CO emissions, the error standard deviations assigned to the prior CO emissions at 7-day and 0.5° resolution are 100%. This value of 100% has already been chosen in Fortems-Cheiney et al. [2011] and in Fortems-Cheiney et al. [2012]. For this CO illustration, the covariance matrix \mathbf{B} of the prior errors is defined as diagonal (i.e. only variances in the individual control variables listed in 4.2.1 are taken into account). With such a set-up, in theory, we could obtain negative posterior emissions since the inversion system does not impose a constraint of positivity in the results. Nevertheless, even an uncertainty of 100% leads to a prior distribution mostly (>80%) on the positive side. The assimilation of data showing an increase above the background (at the edges of the domain; not shown) further drive the inversion towards positive emissions for both CO and NO_x inversions. In practice, our inversion does not lead to negative posterior emissions (Figure 7b). Spatial and temporal correlations in \mathbf{B} would further limit the probability to get negative emissions locally by smoothing the posterior emissions at a spatial scale at which the “aggregated” prior uncertainty is smaller than 100%. However, a positivity constraint should be implemented in future versions of the system.

552 Based on the sensitivity test in Figure 4, the errors assigned to the CO lateral boundary conditions
553 and to their initial conditions are set at 15%. As these relative errors are significantly lower than
554 those for the emissions and as variations in the CO surface concentrations are mainly driven by
555 emissions (Figure 3), we assume a small relative influence of the correction of initial and boundary
556 conditions on our results. The variance of the individual observation errors in \mathbf{R} is defined as the
557 quadratic sum of the measurement error reported in the MOPITT and the OMI data sets, and of the
558 CTM errors (including chemistry and transport errors and representativity errors) set at 20% of the
559 retrieval values. The representativity errors could have been reduced with the choice of a finer CTM
560 resolution (e.g., with a resolution closer to the size of the satellite pixel). Error correlations between
561 the super-observations are neglected, so that the covariance matrix \mathbf{R} of the observation errors is
562 diagonal.

563

4.2.3. Inversion of CO emissions

564

565 Ten iterations are needed to reduce the norm of the gradient of J by 90% with the minimization
566 algorithm M1QN3 and obtain the increments, i.e. the corrections provided by the inversion. The
567 prior CO emissions over Europe for the first week of March 2015 and their increments are shown in
568 Figure 7. As expected from the large differences (Figure 5d) between the prior surface
569 concentrations (Figure 5a) and the MOPITT observations (Figure 5b), local increments can reach
570 more than +50% (Figure 7b). CO emissions are increased over Central and Eastern Europe, except
571 in the south of Poland. On the contrary, CO emissions are decreased over Spain and Portugal. The
572 analyzed concentrations are the concentrations simulated by CHIMERE with the posterior fluxes: as
573 expected, the optimization of the fluxes improves the fit of the simulated concentrations to the
574 observations (Figure 5c and Figure 5e), particularly over Central and Eastern Europe. Over this area
575 (see the purple box in Figure 5), the mean bias between the simulation and the observations has
576 been reduced by about 27% when using the posterior emissions (mean bias of 11.6 ppbv against
577 15.9 ppbv with the prior emissions, Table 4). The RMSE and the standard deviation have been
578 reduced by about 50% and the correlation has been strongly improved (0.74 when using the
579 posterior emissions against 0.02).

580

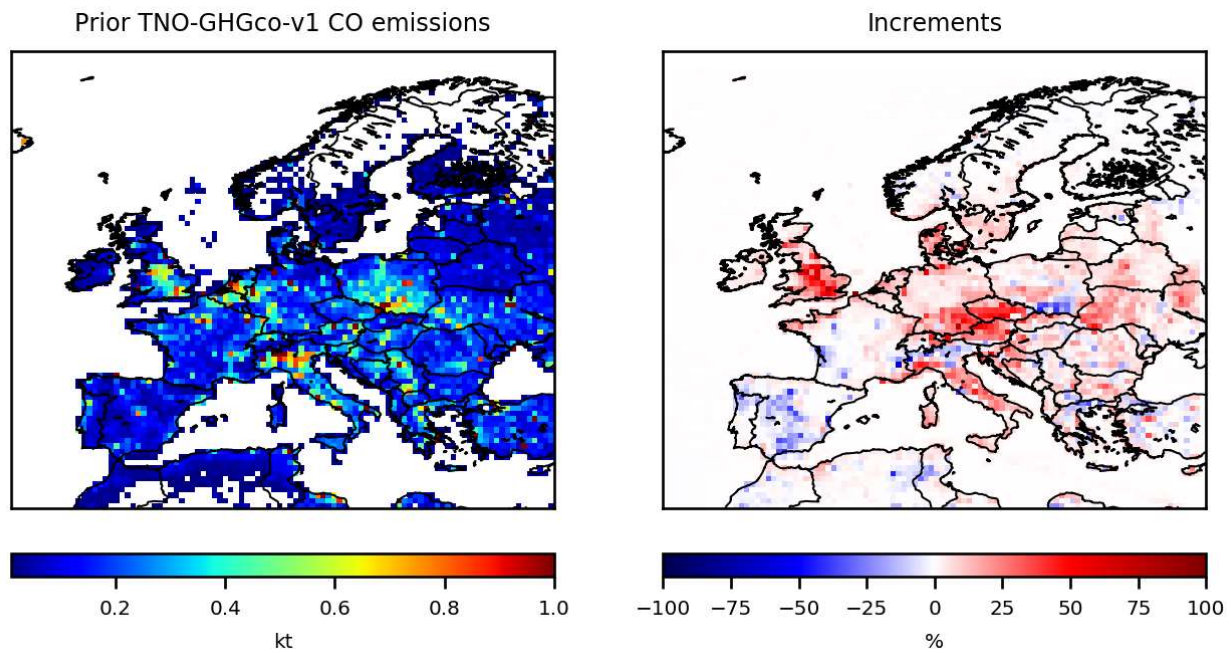


Figure 7. a) TNO-GHGco-v1 CO anthropogenic prior emissions, in ktCO/grid-cell and b) increments provided by the inversion with constraints from MOPITTv8-NIR-TIR from the 1st to the 7th, March 2015, in %.

prior				posterior			
MB	RMSE	STD	r	MB	RMSE	STD	r
15.88	41.95	38.82	0.02	11.58	21.14	17.69	0.74
			(p value = 0.99)				(p value = 2.08×10^{-11})

Table 4. Statistics for the comparison between simulated and observed CO surface concentrations over Central and Eastern Europe (see the area in purple in Figure 5). MB= Mean Bias, RMSE= Root Mean Square Error, STD= Standard Deviation are in ppbv. The spatial correlations r are presented with their p value.

4.2.4. Inversion of NO_x emissions

The prior NO_x emissions and the corrections provided by the different sensitivity tests of Table 3 are shown in Figure 8. Here, we analyzed the results from inversion E. As expected from the underestimation of the prior tropospheric columns in Figure 6a, local increments may be large, for example over industrial areas (e.g., over the Po Valley) and over the Netherlands, with increments of more than +50% (Figure 8b). The analyzed NO₂ tropospheric columns in Figure 6c are the columns simulated by CHIMERE with the NO₂ posterior fluxes: as expected, the optimization of the fluxes improves the fit of the simulated concentrations to the observations over the Netherlands (Figure 6e). Over this area (see the purple box in Figure 6), where the OMI uncertainties are lower

599 than 50% (Figure 9b), the mean bias between the simulation and the observations has been reduced
600 by about 24% when using the posterior emissions (mean bias of 1.9×10^{15} molec.cm⁻² against
601 2.6×10^{15} molec.cm⁻² with the prior emissions, Table 5, Figure 9a). The RMSE and the standard
602 deviation have been reduced by about 7%. The correlation has not been improved.

603

604 Even with high emission increments, the impact on the tropospheric columns is rather small. We
605 have performed a test to explain this lack of sensitivity. We have simulated NO₂ columns with
606 anthropogenic emissions increased by a factor 3 compared to the simulation in Figure 6a. The ratio
607 between these two simulations shows strong non-linearities, blurring the multiplicative effect of our
608 increments and explaining the lack of sensitivity (not shown). By increasing NO_x anthropogenic
609 emissions, NO₂ tropospheric columns can be strongly increased and can even exceed the
610 observations values for particular pixels. NO₂ tropospheric columns can also be decreased or only
611 slightly increased. On average, it tends to increase the concentrations by a factor that is much
612 smaller than the factor of increase in the anthropogenic emissions. However, the patterns where the
613 posterior tropospheric columns exceed the observations or, on the opposite are decreased or only
614 slightly increased, explain why the inversion system does not attempt at increasing further the
615 average level of the concentration (to decrease further the general bias to the observations), even
616 though it accounts for the impact of non-linearities in the chemistry through the use of the M1QN3
617 minimization algorithm. We can conclude that the strong non-linearities of the NO_x chemistry
618 mainly explain the lack of sensitivity between NO_x emissions and satellite NO₂ columns. Besides
619 chemical effects, the lack of sensitivity could be also partly due to the contribution of emissions
620 during the preceding days and the assimilation window will be widened in the near future.

621

622 The posterior emissions and their uncertainties will have to be evaluated and may bring hints to the
623 cause of the discrepancies between simulated and observed NO₂ tropospheric columns. The biases
624 between OMI and simulated NO₂ tropospheric columns are a complex topic that is not related to our
625 CHIMERE simulations only [Huijnen et al., 2010; Souri et al., 2020; Elguindi et al., 2020]. Several
626 studies have indeed already reported that strong non-linear relationships exist between NO_x
627 emissions and satellite NO₂ columns [Lamsal et al., 2011; Vinken et al., 2014; Miyazaki et al.,
628 2017; Li and Wang, 2019]. This reveals that a fully comprehensive scientific study is required, by
629 analyzing the NO_x lifetime through processes such as the NO₂+OH reactions and/or the reactive
630 uptake of NO₂ and N₂O₅ by aerosols [e.g. Lin et al., 2012; Stavrou et al., 2013].

631

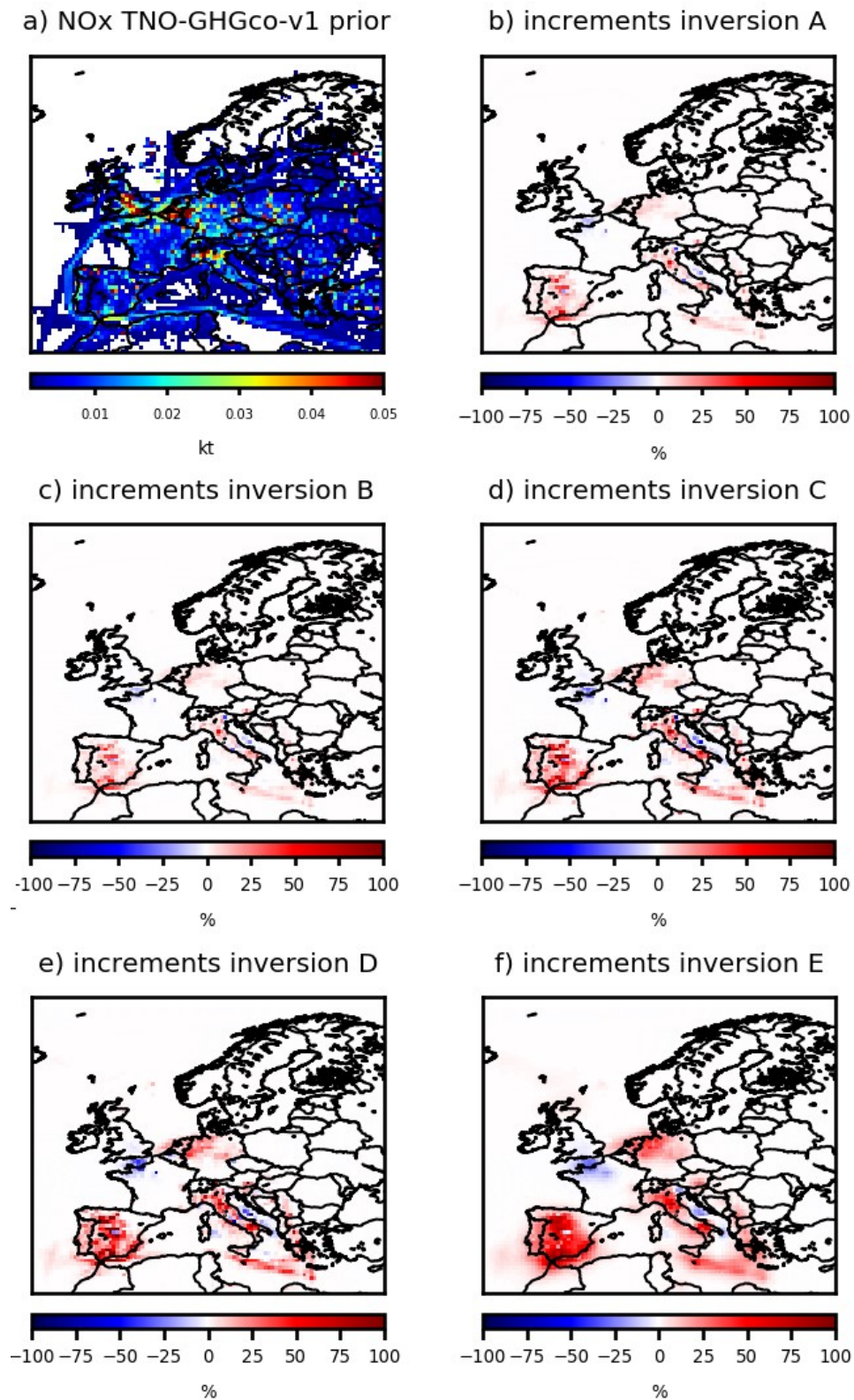


Figure 8. a) TNO-GHGco-v1 NO_x anthropogenic prior emissions, in ktNO₂/grid-cell and increments provided by the inversion b) A, c) B, d) C, e) D and f) E with constraints from OMI the 19th, February 2015, in %. The description of the different inversions is given in Table 3.

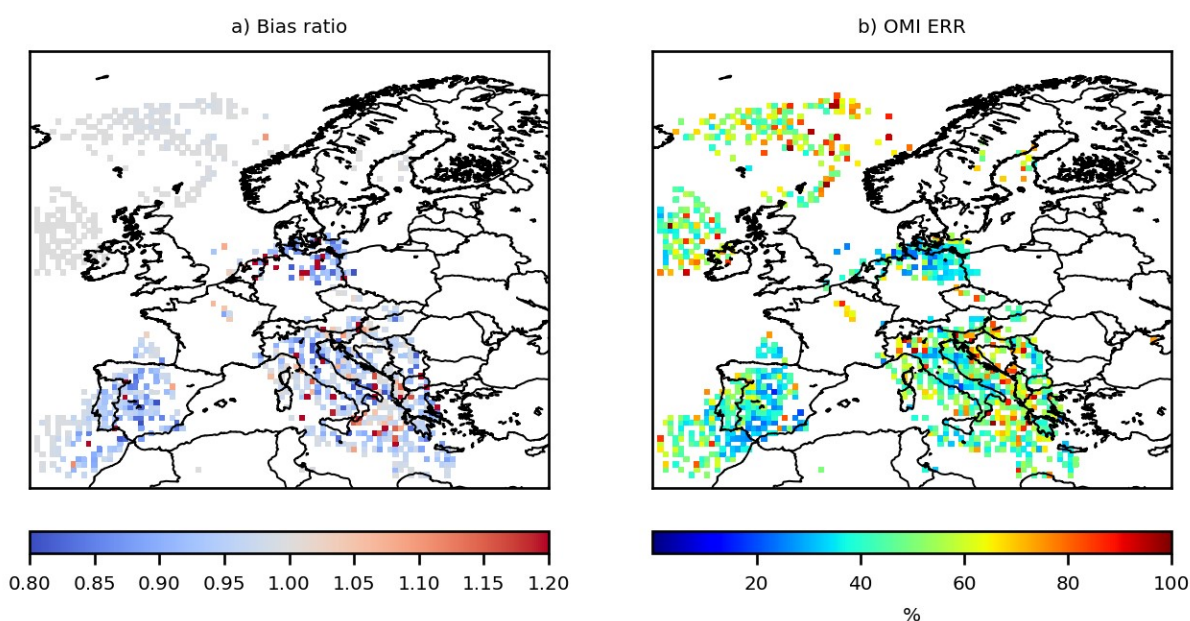


Figure 9. a) Bias ratio between CHIMERE simulations using the posterior emissions against prior TNO-GHGco-v1 emissions compared to the OMI-QA4ECV-v1.1 observations. All ratios lower than 1, in blue, demonstrate that posterior emissions improve the simulation compared to the prior ones. b) OMI uncertainties, in %, the 19th, February 2015.

	prior				posterior			
	MB	RMSE	STD	r	MB	RMSE	STD	r
NO ₂	2.6x10 ¹⁵	4.0x10 ¹⁵	3.0x10 ¹⁵	0.008 (p=0.96)	1.9x10 ¹⁵	3.74x10 ¹⁵	2.9x10 ¹⁵	0.01 (p=0.91)

Table 5. Statistics for the comparison between simulated and observed NO₂ tropospheric columns for the inversion E, mainly over the Netherlands (see the area in purple in Figure 6). MB= Mean Bias, RMSE= Root Mean Square Error, STD= Standard Deviation are in molec_m.cm⁻². The spatial correlations *r* are presented with their *p* value.

5. Conclusion/Discussion

This paper presents the Bayesian variational inverse system PYVAR-CHIMERE, which has been adapted to the inversion of reactive species such as CO and NO_x, taking advantage of the previous developments for long-lived species such as CO₂ [Broquet et al., 2011] and CH₄ [Pison et al., 2018]. We show the potential of PYVAR-CHIMERE, with inversions for CO and NO_x illustrated over Europe. PYVAR-CHIMERE will now be used to infer CO and NO_x emissions over long periods, e.g. first for a whole season or year and then for the recent decade 2005-2015 in the framework of the H2020 VERIFY project over Europe, and in the framework of the ANR PolEASIA project over China, to quantify their trend and their spatio-temporal variability. Nevertheless, as we have reported strong non-linear relationships between NO_x emissions and

653 satellite NO₂ columns, a fully comprehensive scientific study is required, by analyzing the NO_x
654 lifetime through processes such as the NO₂+OH reactions and/or the reactive uptake of NO₂ and
655 N₂O₅ by aerosols [e.g. Lin et al., 2012; Stavrakou et al., 2013]. Biogenic emissions will be also
656 further studied to better understand the relationship between NO_x emissions and NO₂ spaceborne
657 columns.

658

659 The PYVAR-CHIMERE system can handle any large number of both control parameters and
660 observations. It will be able to cope with the dramatic increase in the number of data in the near
661 future with, for example, the high-resolution imaging (pixel of 7x3.5 km²) of the new Sentinel-
662 5P/TROPOMI program, launched in October 2017. These new space missions with high-resolution
663 imaging have the ambition to monitor atmospheric chemical composition for the quantification of
664 anthropogenic emissions. It will indeed entail using PYVAR-CHIMERE at higher spatio-temporal
665 resolutions, but probably for smaller domains (i.e., over countries rather than over Europe) as a
666 compromise between resolution and the computational cost. Moreover, a step forward in the joint
667 assimilation of co-emitted pollutants will be possible with the PYVAR-CHIMERE system and the
668 availability of TROPOMI co-localized images of CO and NO₂. This should improve the
669 consistency of the inversion results and can be used to inform inventory compilers, and
670 subsequently improve emission inventories. Moreover, this development will help in further
671 understanding air quality problems and addressing air quality related emissions at the national to
672 subnational scales.

673

674 **Author Contribution**

675 All authors have contributed to the manuscript writing (main authors: AFC, GB, IP and GD) and to
676 the development of the present version of the PYVAR-CHIMERE system (main developer: IP). IP
677 and GD have parallelized the adjoint version from Menut et al., [2000], Menut et al., [2003] and
678 Pison et al., [2007]. IP has complemented the adjoint of new parameterizations since the CHIMERE
679 release in 2011 and the tangent-linear model.

680

681 **Code and Data Availability**

682 OMI QA4ECV NO₂ product can be found here: <http://temis.nl/qa4ecv/no2.html>.
683 MOPITTv8-NIR-TIR CO product can be found here: <ftp://l5ftl01.larc.nasa.gov/MOPITT/>
684 The CHIMERE code is available here: www.lmd.polytechnique.fr/chimere/.

685

686 The associated documentation of PYVAR-CHIMERE is available on the website
687 <https://pyvar.lsce.ipsl.fr/doku.php/3chimere:headpage>. The documentation includes a whole
688 description of PYVAR-CHIMERE and several tutorials on how to run a first PYVAR-CHIMERE
689 simulation or how to run an inversion.

690

691 **Competing interests**

692 The authors declare that they have no conflict of interest.

693
694
695
696
697
698
699
700
701
702
703
704
705
706
707
708
709
710
711
712
713
714
715
716
717
718
719
720
721
722
723
724
725
726
727
728
729
730
731
732
733
734
735
736
737
738
739
740
741
742
743
744

Acknowledgements

We acknowledge L. Menut and C. Schmechtig for their contributions to the development work on the adjoint code of CHIMERE and its parallelization. We acknowledge the TNO team (H.A. Denier van der Gon, J. Kuenen, S. Dellaert, S. Jonkers, A. Visschedijk, et al.) for providing NO_x and CO emissions over Europe. We also acknowledge the free use of tropospheric NO₂ column data from the OMI sensor from <http://temis.nl/qa4ecv/no2.html> and the free use of CO surface concentrations from the MOPITT sensor from <ftp://15ftl01.larc.nasa.gov/MOPITT/>. For this study, A. Fortems-Cheiney was funded by the French Space Agency-Centre National d'Etudes Spatiales CNES and by the H2020 VERIFY project, funded by the European Commission Horizon 2020 research and innovation programme, under agreement number 776810. L. Costantino was funded by the PolEASIA ANR project under the allocation ANR-15-CE04-0005. This work was granted access to the HPC resources of TGCC under the allocations A0050107232 and A0070102201 made by GENCI. Finally, we wish to thank F. Marabelle (LSCE) and his team for computer support.

References

- Aumont, B., Chervier, F., and Laval, S.: Contribution of HONO sources to the NO_x/HO_x/O₃ chemistry in the polluted boundary layer. *Atmospheric Environment*, 37(4):487 – 498, 2003.
- Belikov, D. A., Maksyutov, S., Yaremchuk, A., Ganshin, A., Kaminski, T., Blessing, S., Sasakawa, M., Gomez-Pelaez, A. J., and Starchenko, A.: Adjoint of the global Eulerian–Lagrangian coupled atmospheric transport model (A-GELCA v1.0): development and validation, *Geosci. Model Dev.*, 9, 749–764, <https://doi.org/10.5194/gmd-9-749-2016>, 2016.
- Boersma, K. F., Vinken, G. C. M., and Eskes, H. J.: Representativeness errors in comparing chemistry transport and chemistry climate models with satellite UV–Vis tropospheric column retrievals, *Geosci. Model Dev.*, 9, 875–898, <https://doi.org/10.5194/gmd-9-875-2016>, 2016.
- Boersma, K. F., Eskes, H., Richter, A., De Smedt, I., Lorente, A., Beirle, S., Van Geffen, J., Peters, E., Van Roozendaal, M. and Wagner, T.: QA4ECV NO₂ tropospheric and stratospheric vertical column data from OMI (Version 1.1) [Data set], Royal Netherlands Meteorological Institute (KNMI), <http://doi.org/10.21944/qa4ecv-no2-omi-v1.1>, 2017.
- Bousquet, P., P. Ciais, P. Peylin, M. Ramonet, and P. Monfray: Inverse modeling of annual atmospheric CO₂ sources and sinks: 1. Method and control inversion, *J. Geophys. Res.*, 104(D21), 26,161 – 26,178, doi:10.1029/1999JD900342, 1999.
- Broquet, G., Chevallier, F., Rayner, P., Aulagnier, C., Pison, I., Ramonet, M., Schmidt, M., Vermeulen, A. T., and Ciais, P.: A European summertime CO₂ biogenic flux inversion at mesoscale from continuous in situ mixing ratio measurements, *J. Geophys. Res.*, 116, D23303, doi: 10.1029/2011JD016202, 2011.
- Broquet, G., Chevallier, F., Bréon, F.-M., Kadyrov, N., Alemanno, M., Apadula, F., Hammer, S., Haszpra, L., Meinhardt, F., Morguí, J. A., Necki, J., Piacentino, S., Ramonet, M., Schmidt, M., Thompson, R. L., Vermeulen, A. T., Yver, C., and Ciais, P.: Regional inversion of CO₂ ecosystem fluxes from atmospheric measurements: reliability of the uncertainty estimates, *Atmos. Chem. Phys.*, 13, 9039–9056, <https://doi.org/10.5194/acp-13-9039-2013>, 2013.
- Chevallier, F., M. Fisher, P. Peylin, S. Serrar, P. Bousquet, F.-M. Bréon, A. Chédin, and P. Ciais: Inferring CO₂ sources and sinks from satellite observations: method and application to TOVS data, *J. Geophys. Res.*, 110, D24309, [doi:10.1029/2005JD006390](https://doi.org/10.1029/2005JD006390), 2005.

Chevallier, F., F.-M. Bréon, and P. J. Rayner: The contribution of the Orbiting Carbon Observatory to the estimation of CO₂ sources and sinks: Theoretical study in a variational data assimilation framework. *J. Geophys. Res.*, 112, D09307, [doi:10.1029/2006JD007375](https://doi.org/10.1029/2006JD007375), 2007.

Chevallier, F., Ciais, P., Conway, T. J., Aalto, T., Anderson, B. E., Bousquet, P., Brunke, E. G., Ciattaglia, L., Esaki, Y., Fröhlich, M., Gomez, A., Gomez-Pelaez, A. J., Haszpra, L., Krummel, P. B., Langenfelds, R. L., Leuenberger, M., Machida, T., Maignan, F., Matsueda, H., Morguí, J. A., Mukai, H., Nakazawa, T., Peylin, P., Ramonet, M., Rivier, L., Sawa, Y., Schmidt, M., Steele, L. P., Vay, S. A., Vermeulen, A. T., Wofsy, S., and Worthy, D.: CO₂ surface fluxes at grid point scale estimated from a global 21 year reanalysis of atmospheric measurements, *J. Geophys. Res.*, 115, 1–17, <https://doi.org/10.1029/2010jd013887>, 2010.

Ciarelli, G., Theobald, M. R., Vivanco, M. G., Beekmann, M., Aas, W., Andersson, C., Bergstrom, R., Manders-Groot, A., Couvidat, F., Mircea, M., Tsyro, S., Fagerli, H., Mar, K., Raffort, V., Roustan, Y., Pay, M.-T., Schaap, M., Kranenburg, R., Adani, M., Briganti, G., Cappelletti, A., D'Isidoro, M., Cuvelier, C., Cholakian, A., Bessagnet, B., Wind, P., and Colette, A.: Trends of inorganic and organic aerosols and precursor gases in Europe: insights from the EURODELTA multi-model experiment over the 1990-2010 period, *Geosci. Model Dev.*, 12, 4923–4954, <https://doi.org/10.5194/gmd-12-4923-2019>, 2019.

CHIMERE documentation, <https://www.lmd.polytechnique.fr/chimere/docs/CHIMEREdoc2017.pdf>, Last update of this documentation: June 8, 2017, 2017.

Deeter, M. N., Edwards, D. P., Francis, G. L., Gille, J. C., Mao, D., Martínez-Alonso, S., Worden, H. M., Ziskin, D., and Andreae, M. O.: Radiance-based retrieval bias mitigation for the MOPITT instrument: the version 8 product, *Atmos. Meas. Tech.*, 12, 4561–4580, <https://doi.org/10.5194/amt-12-4561-2019>, 2019.

Ding, J., Miyazaki, K., van der A, R. J., Mijling, B., Kurokawa, J.-I., Cho, S., Janssens-Maenhout, G., Zhang, Q., Liu, F., and Levelt, P. F.: Intercomparison of NO_x emission inventories over East Asia, *Atmos. Chem. Phys.*, 17, 10125–10141, <https://doi.org/10.5194/acp-17-10125-2017>, 2017.

EEA, Air quality in Europe - 2018 report, 12/2018, <https://www.eea.europa.eu/publications/air-quality-in-europe-2018>.

Elbern, H., Strunk, A., Schmidt, H., and Talagrand, O.: Emission rate and chemical state estimation by 4-dimensional variational inversion, *Atmos. Chem. Phys.*, 7, 3749–3769, <https://doi.org/10.5194/acp-7-3749-2007>, 2007.

Elguindi, N., Granier, C., Stavrakou, T., Darras, S., Bauwens, M., Cao, H., et al.: Intercomparison of magnitudes and trends in anthropogenic surface emissions from bottom-up inventories, top-down estimates, and emission scenarios. *Earth's Future*, 8, e2020EF001520, <https://doi.org/10.1029/2020EF001520>, 2020.

EMEP/EEA air pollutant emission inventory guidebook, 2016.

794
795
796
797
798
799
800
801
802
803
804
805
806
807
808
809
810
811
812
813
814
815
816
817
818
819
820
821
822
823
824
825
826
827
828
829
830
831
832
833
834
835
836
837
838
839
840
841
842
843
844
845

EMEP/CEIP,

https://ceip.at/ms/ceip_home1/ceip_home/webdab_emepdatabase/emissions_emepmodels/

de Foy, B., Lu, Z. and Streets, D.G.: Satellite NO₂ retrievals suggest China has exceeded its NO_x reduction goals from the twelfth Five-Year Plan, *Nature Scientific Reports*, 6:35912, 2016.

Fortems-Cheiney, A., et al: Ten years of CO emissions as seen from MOPITT, *Journal of Geophysical Research*, 116, D5, <https://doi.org/10.1029/2010JD014416>, 2011.

Fortems-Cheiney, A., Chevallier, F., Pison, I., Bousquet, P., Saunois, M., Szopa, S., Cressot, C., Kurosu, T. P., Chance, K., and Fried, A.: The formaldehyde budget as seen by a global-scale multi-constraint and multi-species inversion system, *Atmos. Chem. Phys.*, 12, 6699–6721, <https://doi.org/10.5194/acp-12-6699-2012>, 2012.

Gilbert, J., and C. Lemaréchal (1989), Some numerical experiments with variable storage quasi Newton algorithms, *Math. Program.*, 45, 407–435.

Guenther, A., Karl, T., Harley, P., Wiedinmyer, C., Palmer, P. I., and Geron, C.: Estimates of global terrestrial isoprene emissions using MEGAN (Model of Emissions of Gases and Aerosols from Nature), *Atmos. Chem. Phys.*, 6, 3181–3210, <https://doi.org/10.5194/acp-6-3181-2006>, 2006.

Hakami, A., Henze, D. K., Seinfeld, J. H., Singh, K., Sandu, A., Kim, S., Byun, D., and Li, Q.: The adjoint of CMAQ, *Environ. Sci. Technol.*, 41, 7807–7817, <https://doi.org/10.1021/es070944p>, 2007.

Hein, R., et coll.: An inverse modeling approach to investigate the global atmospheric methane cycle, *Global. Biogeochem. Cycles*, 11, 43-76, 1997.

Henze, D. K., Hakami, A., and Seinfeld, J. H.: Development of the adjoint of GEOS-Chem, *Atmos. Chem. Phys.*, 7, 2413–2433, <https://doi.org/10.5194/acp-7-2413-2007>, 2007.

Huijnen, V., Eskes, H. J., Poupkou, A., Elbern, H., Boersma, K. F., Foret, G., Sofiev, M., Valdebenito, A., Flemming, J., Stein, O., Gross, A., Robertson, L., D'Isidoro, M., Kioutsioukis, I., Frieze, E., Amstrup, B., Bergstrom, R., Strunk, A., Vira, J., Zyryanov, D., Maurizi, A., Melas, D., Peuch, V.-H., and Zerefos, C.: Comparison of OMI NO₂ tropospheric columns with an ensemble of global and European regional air quality models, *Atmos. Chem. Phys.*, 10, 3273–3296, <https://doi.org/10.5194/acp-10-3273-2010>, 2010.

Hooghiemstra, P. B., Krol, M. C., Bergamaschi, P., de Laat, A. T. J., van der Werf, G. R., Novelli, P.C., Deeter, M. N., Aben, I., and Rockmann, T.: Comparing optimized CO emission estimates using MOPITT or NOAA surface network observations, *J. Geophys. Res.*, 117, D06309, doi:10.1029/2011JD017043, 2012.

Kadyrov, N., Broquet, G., Chevallier, F., Rivier, L., Gerbig, C., and Ciais, P.: On the potential of the ICOS atmospheric CO₂ measurement network for estimating the biogenic CO₂ budget of Europe, *Atmos. Chem. Phys.*, 15, 12765–12787, <https://doi.org/10.5194/acp-15-12765-2015>, 2015.

Konovalov, I. B. et coll.: Inverse modelling of the spatial distribution of NO emissions on a continental scale using satellite data, *Atmos. Chem. Phys.*, 6, 1747-1770, doi:10.5194/acp-6-1747-2006, 2006.

Konovalov, I. B., Beekmann, M., Burrows, J. P., and Richter, A.: Satellite measurement based estimates of decadal changes in European nitrogen oxides emissions, *Atmos. Chem. Phys.*, 8, 2623-2641, doi:10.5194/acp-8-2623-2008, 2008.

Konovalov, I. B., Beekmann, M., Richter, A., Burrows, J. P., and Hilboll, A.: Multi-annual changes of NO_x emissions in megacity regions: nonlinear trend analysis of satellite measurement based estimates, *Atmos. Chem. Phys.*, 10, 8481-8498, doi:10.5194/acp-10-8481-2010, 2010.

Koohkan, M. R., Bocquet, M., Roustan, Y., Kim, Y., and Seigneur, C.: Estimation of volatile organic compound emissions for Europe using data assimilation, *Atmos. Chem. Phys.*, 13, 5887-5905, <https://doi.org/10.5194/acp-13-5887-2013>, 2013.

Krol, M. C., Meirink, J. F., Bergamaschi, P., Mak, J. E., Lowe, D., Jöckel, P., Houweling, S., and Röckmann, T.: What can 14CO measurements tell us about OH?, *Atmospheric chemistry and physics*, 8, 5033–5044, 2008.

Kuenen, J. J. P., Visschedijk, A. J. H., Jozwicka, M., and Denier van der Gon, H. A. C.: TNO-MACC_II emission inventory; a multi-year (2003–2009) consistent high-resolution European emission inventory for air quality modelling, *Atmos. Chem. Phys.*, 14, 10963-10976, <https://doi.org/10.5194/acp-14-10963-2014>, 2014.

Kurokawa, J., Ohara, T., Morikawa, T., Hanayama, S., Janssens-Maenhout, G., Fukui, T., Kawashima, K., and Akimoto, H.: Emissions of air pollutants and greenhouse gases over Asian regions during 2000–2008: Regional Emission inventory in ASia (REAS) version 2, *Atmos. Chem. Phys.*, 13, 11019-11058, doi:10.5194/acp-13-11019-2013, 2013.

Kurtenbach, R., Becker, K., Gomes, J., Kleffmann, J., Lžrzer, J., Spittler, M., Wiesen, P., Ackermann, R., Geyer, A., and Platt, U.: Investigations of emissions and heterogeneous formation of HONO in a road traffic tunnel. *Atmospheric Environment*, 35(20):9506 – 9517. 3385D3394, 2001.

Lamsal, L. N., Martin, R. V., Padmanabhan, A., van Donkelaar, A., Zhang, Q., Sioris, C. E., Chance, K., Kurosu, T. P., and Newchurch, M. J.: Application of satellite observations for timely updates to global anthropogenic NO_x emission inventories, *Geophys. Res. Lett.*, 38, L05810, doi:[10.1029/2010GL046476](https://doi.org/10.1029/2010GL046476), 2011.

Lattuati, M., Impact des émissions européennes sur le bilan de l'ozone troposphérique a l'interface de l'europe et de l'atlantique nord : apport de la modélisation lagrangienne et des mesures en altitude, Ph.D. thesis, Université Paris VI, 1997.

Lelieveld, J., Klingmüller, K., Pozzer, A., Pöschl, U., Fnais, M., Daiber, A., Münzel, T.; Cardiovascular disease burden from ambient air pollution in Europe reassessed using novel hazard ratio functions, *European Heart Journal*, , ehz135, <https://doi.org/10.1093/eurheartj/ehz135>, 2019.

Li, J. and Wang, Y.: Inferring the anthropogenic NO_x emission trend over the United States during 2003–2017 from satellite observations: was there a flattening of the emission trend after the Great Recession?, *Atmos. Chem. Phys.*, 19, 15339–15352, <https://doi.org/10.5194/acp-19-15339-2019>, 2019.

- Lin, J.-T., McElroy, M. B., and Boersma, K. F.: Constraint of anthropogenic NO_x emissions in China from different sectors: a new methodology using multiple satellite retrievals, *Atmos. Chem. Phys.*, 10, 63–78, doi:10.5194/acp-10-63-2010, 2010.
- Lin, J.-T., Liu, Z., Zhang, Q., Liu, H., Mao, J., and Zhuang, G.: Modeling uncertainties for tropospheric nitrogen dioxide columns affecting satellite-based inverse modeling of nitrogen oxides emissions, *Atmos. Chem. Phys.*, 12, 12255–12275, <https://doi.org/10.5194/acp-12-12255-2012>, 2012.
- Liu, F., Beirle, S., Zhang, Q., Dörner, S., He, K., and Wagner, T.: NO_x lifetimes and emissions of cities and power plants in polluted background estimated by satellite observations, *Atmos. Chem. Phys.*, 16, 5283–5298, <https://doi.org/10.5194/acp-16-5283-2016>, 2016.
- Locatelli, R., Bousquet, P., Saunio, M., Chevallier, F., and Cressot, C.: Sensitivity of the recent methane budget to LMDz sub-grid-scale physical parameterizations, *Atmos. Chem. Phys.*, 15, 9765–9780, <https://doi.org/10.5194/acp-15-9765-2015>, 2015.
- Mailler S., L. Menut, D. Khvorostyanov, M. Valari, F. Couvidat, G. Siour, S. Turquety, R. Briant, P. Tuccella, B. Bessagnet, A. Colette, L. Letinois, and F. Meleux, CHIMERE-2017: from urban to hemispheric chemistry-transport modeling, *Geosci. Model Dev.*, 10, 2397–2423, <https://doi.org/10.5194/gmd-10-2397-2017>, 2017.
- Menut, L., R. Vautard, M. Beekmann, and C. Honoré: Sensitivity of photochemical pollution using the adjoint of a simplified chemistry-transport model, *J. Geophys. Res.*, 105, 15,379–15,402, 2000.
- Menut L.: Adjoint modelling for atmospheric pollution processes sensitivity at regional scale during the ESQUIF IOP2, *Journal of Geophysical Research - Atmospheres*, 108, D17, <https://doi.org/10.1029/2002JD002549>, 2003.
- Menut, L., Goussebaile, A., Bessagnet, B., Khvorostyanov, D., and Ung, A.: Impact of realistic hourly emissions profiles on air pollutants concentrations modelled with CHIMERE, *Atmospheric Environment*, 49, 233–244, doi:10.1016/j.atmosenv.2011.11.057, 2012.
- Menut, L., Bessagnet, B., Khvorostyanov, D., Beekmann, M., Blond, N., Colette, A., Coll, I., Curci, G., Foret, G., Hodzic, A., Mailler, S., Meleux, F., Monge, J.-L., Pison, I., Siour, G., Turquety, S., Valari, M., Vautard, R., and Vivanco, M. G.: CHIMERE 2013: a model for regional atmospheric composition modelling, *Geosci. Model Dev.*, 6, 981–1028, doi:10.5194/gmd-6-981-2013, 2013.
- Menut, L., Bessagnet, B., Siour, G., Mailler, S., Pennel, R. and Cholakian, A. : Impact of lockdown measures to combat Covid-19 on air quality over western Europe, *Science of The Total Environment*, 741, <https://doi.org/10.1016/j.scitotenv.2020.140426>, 2020.
- Mijling, B., and R. J. van der A: Using daily satellite observations to estimate emissions of short-lived air pollutants on a mesoscopic scale, *J. Geophys. Res.*, 117, D17302, doi:10.1029/2012JD017817, 2012.
- Mijling, B., et al., Regional nitrogen oxides emission trends in East Asia observed from space, *Atmos. Chem. Phys.*, 3, 12003, 2013.

Miyazaki, K., Eskes, H., Sudo, K., Boersma, K. F., Bowman, K., and Kanaya, Y.: Decadal changes in global surface NO_x emissions from multi-constituent satellite data assimilation, *Atmos. Chem. Phys.*, 17, 807–837, <https://doi.org/10.5194/acp-17-807-2017>, 2017.

Muller, J.-P., Kharbouche, S., Gobron, N., Scanlon, T., Govaerts, Y., Danne, O., Schultz, J., Lattanzio, A., Peters, E., De Smedt, I., Beirle, S., Lorente, A., Coheur, P. F., George, M., Wagner, T., Hilboll, A., Richter, A., Van Roozendael, M., and Boersma, K. F.: Recommendations (scientific) on best practices for retrievals for Land and Atmosphere ECVs (QA4ECV Deliverable 4.2 version 1.0), 186 pp., available at: <http://www.qa4ecv.eu/sites/default/files/D4.2.pdf> (last access: 12 April 2018), 2016.

Owens, R. G. and Hewson, T.: ECMWF Forecast User Guide, Reading, <https://doi.org/10.21957/m1cs7h>, <https://software.ecmwf.int/wiki/display/FUG/Forecast+User+Guide>, 2018.

Pétron, G., Granier, C., Khattatov, B., Lamarque, J.F., Yudin, V., Muller, J.F. and Gille, J.: Inverse modeling of carbon monoxide surface emissions using CMDL networks observations, *J. Geophys. Res.*, 107, D24, 2002.

Pison, I., Menut, L., and Bergametti, G.: Inverse modeling of surface NO_x anthropogenic emission fluxes in the Paris area during the ESQUIF campaign, *J. Geophys. Res. Atmos.*, 112, D24302, doi:10.1029/2007JD008871, 2007.

Pison, I., Bousquet, P., Chevallier, F., Szopa, S., and Hauglustaine, D.: Multi-species inversion of CH₄, CO and H₂ emissions from surface measurements, *Atmospheric Chemistry and Physics*, 9, 5281–5297, 2009.

Pison, I., Berchet, A., Saunois, M., Bousquet, P., Broquet, G., Conil, S., Delmotte, M., Ganesan, A., Laurent, O., Martin, D., O'Doherty, S., Ramonet, M., Spain, T. G., Vermeulen, A., and Yver Kwok, C.: How a European network may help with estimating methane emissions on the French national scale, *Atmos. Chem. Phys.*, 18, 3779–3798, <https://doi.org/10.5194/acp-18-3779-2018>, 2018.

Qu, Z., Henze, D. K., Cooper, O. R., and Neu, J. L.: Improving NO₂ and ozone simulations through global NO_x emission inversions, *Atmos. Chem. Phys. Discuss.*, <https://doi.org/10.5194/acp-2020-307>, in review, 2020.

Rayner, P. J., Michalak, A. M., and Chevallier, F.: Fundamentals of data assimilation applied to biogeochemistry, *Atmos. Chem. Phys.*, 19, 13911–13932, <https://doi.org/10.5194/acp-19-13911-2019>, 2019.

Souri, A. H., Nowlan, C. R., González Abad, G., Zhu, L., Blake, D. R., Fried, A., Weinheimer, A. J., Wisthaler, A., Woo, J.-H., Zhang, Q., Chan Miller, C. E., Liu, X., and Chance, K.: An inversion of NO_x and non-methane volatile organic compound (NMVOC) emissions using satellite observations during the KORUS-AQ campaign and implications for surface ozone over East Asia, *Atmos. Chem. Phys.*, 20, 9837–9854, <https://doi.org/10.5194/acp-20-9837-2020>, 2020.

Stavrakou, T. and J.-F. Müller: Grid-based versus big region approach for inverting CO emissions using Measurement of Pollution in the Troposphere (MOPITT) data, *Journal of Geophysical Research: Atmospheres*, 111, D15, 2006.

- 995 Stavrakou, T., Muller, J.-F., Boersma, K. F., De Smedt, I., and van der A, R. J.: Assessing
 996 the distribution and growth rates of NO_x emission sources by inverting a 10-year record of NO₂
 997 satellite columns, *Geophys. Res. Lett.*, 35, 1–5, doi:10.1029/2008GL033521, 2008.
- 998
 999 Stavrakou, T., Müller, J.-F., Boersma, K. F., van der A, R. J., Kurokawa, J., Ohara, T.,
 1000 and Zhang, Q.: Key chemical NO_x sink uncertainties and how they influence top-down emissions of
 1001 nitrogen oxides, *Atmos. Chem. Phys.*, 13, 9057–9082, <https://doi.org/10.5194/acp-13-9057-2013>,
 1002 2013.
- 1003
 1004 Super, I., Dellaert, S. N. C., Visschedijk, A. J. H., and Denier van der Gon, H. A. C.:
 1005 Uncertainty analysis of a European high-resolution emission inventory of CO₂ and CO to support
 1006 inverse modelling and network design, *Atmos. Chem. Phys.*, 20, 1795–1816,
 1007 <https://doi.org/10.5194/acp-20-1795-2020>, 2020.
- 1008
 1009 Szopa, S., Foret, G., Menut, L., and Cozic, A.: Impact of large scale circulation on
 1010 European summer surface ozone: consequences for modeling, *Atmospheric Environment*, 43, 1189–
 1011 1195, doi:10.1016/j.atmosenv.2008.10.039, 2008.
- 1012
 1013 Talagrand, O. : Assimilation of observations : an introduction, *J. Met. Soc., Japan*, 75,
 1014 191-209, 1997.
- 1015
 1016 Tang, X., Zhu J., Wang Z. F., Wang M., Gbaguidi A., Li J., Shao M., Tang G. Q., and Ji D. S.:
 1017 Inversion of CO emissions over Beijing and its surrounding areas with ensemble Kalman filter,
 1018 *Atmospheric Environment*, 81, 676-686, 2013.
- 1019
 1020 Valin, L. C., Russell, A. R., and Cohen, R. C.: Variations of OH radical in an urban
 1021 plume inferred from NO₂ column measurements, *Geophys. Res. Lett.*, 40, 1856–1860,
 1022 doi:10.1002/grl.50267, 2013.
- 1023
 1024 van der A, R. J., Eskes, H. J., Boersma, K. F., van Noije, T. P. C., van Roozendael, M., De
 1025 Smedt, I., Peters, D. H. M. U., and Meijer, E. W.: Trends, seasonal variability and dominant NO_x
 1026 source derived from a ten year record of NO₂ measured from space, *J. Geophys. Res.*, 113, 1–12,
 1027 doi:10.1029/2007JD009021, 2008.
- 1028
 1029 Vestreng, V., Breivik, K., Adams, M., Wagner, A., Goodwin, J., Rozovskaya, O.,
 1030 and Oacyna, J.: Inventory Review 2005 - Emission Data reported to CLRTAP and under the NEC
 1031 Directive - Initial review for HMs and POPs .EMEP Status report, Norwegian Meteorological
 1032 Institute, Oslo, 2005.
- 1033
 1034 Vinken, G. C. M., Boersma, K. F., Maasakkers, J. D., Adon, M., and Martin, R. V.:
 1035 Worldwide biogenic soil NO_x emissions inferred from OMI NO₂ observations, *Atmos. Chem.*
 1036 *Phys.*, 14, 10363–10381, <https://doi.org/10.5194/acp-14-10363-2014>, 2014.
- 1037
 1038 Yin, Y., Chevallier, F., Ciais, P., Broquet, G., A. Fortems-Cheiney, Pison, I. and Saunois,
 1039 M: Decadal trends in global CO emissions as seen by MOPITT, *Atmos. Chem. Phys.*, 15, 13433-
 1040 13451, 2015.
- 1041
 1042 Yumimoto, K. and Uno, I.: Adjoint inverse modeling of CO emissions over Eastern Asia
 1043 using four-dimensional variational data assimilation, *Atmospheric Environment*, 40, 35, 6836-6845,
 1044 DOI: 10.1016/j.atmosenv.2006.05.042, 2006.
- 1045

1046 Wang, Y., G. Broquet, P. Ciais, F. Chevallier, F. Vogel, N. Kadygrov, L. Wu, Y. Yin, R.
1047 Wang and S. Tao: Estimation of observation errors for large-scale atmospheric inversion of
1048 CO₂ emissions from fossil fuel combustion, *Tellus B: Chemical and Physical Meteorology*, 69:1,
1049 DOI: [10.1080/16000889.2017.1325723](https://doi.org/10.1080/16000889.2017.1325723), 2017.

1050
1051 Wang, Y., Broquet, G., Ciais, P., Chevallier, F., Vogel, F., Wu, L., Yin, Y., Wang, R., and
1052 Tao, S.: Potential of European ¹⁴CO₂ observation network to estimate the fossil fuel CO₂ emissions
1053 via atmospheric inversions, *Atmos. Chem. Phys.*, 18, 4229–4250, [https://doi.org/10.5194/acp-18-](https://doi.org/10.5194/acp-18-4229-2018)
1054 4229-2018, 2018.

1055
1056 WHO World Health Organization: Ambient Air Pollution: a global assessment of
1057 exposure and burden of disease, 2016.

1058
1059 Zheng, T., French, N. H. F., and Baxter, M.: Development of the WRF-CO₂ 4D-Var
1060 assimilation system v1.0, *Geosci. Model Dev.*, 11, 1725–1752, [https://doi.org/10.5194/gmd-11-](https://doi.org/10.5194/gmd-11-1725-2018)
1061 1725-2018, 2018.

1062
1063 Zheng, B., Chevallier, F., Yin, Y., Ciais, P., Fortems-Cheiney, A., Deeter, M. N., Parker,
1064 R. J., Wang, Y., Worden, H. M., and Zhao, Y.: Global atmospheric carbon monoxide budget 2000–
1065 2017 inferred from multi-species atmospheric inversions, *Earth Syst. Sci. Data*, 11, 1411–1436,
1066 <https://doi.org/10.5194/essd-11-1411-2019>, 2019.